TECHNICAL REPORT S-78-14

NON-NORMAL IMPACT AND PENETRATION: ANALYSIS FOR HARD TARGETS AND SMALL ANGLES OF ATTACK
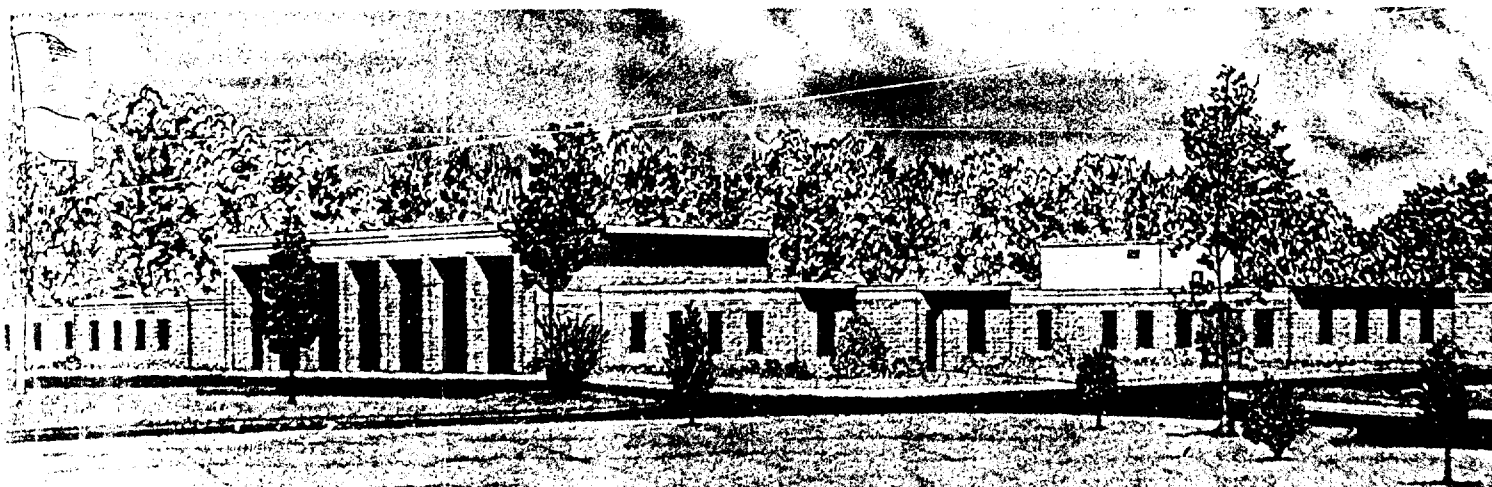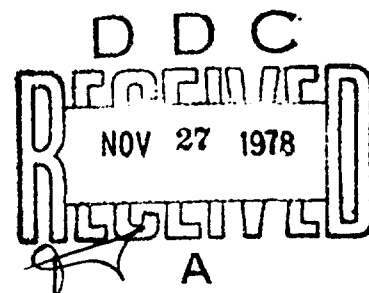
by

Robert S. Bernard, Daniel C. Creighton

Soils and Pavements Laboratory
U. S. Army Engineer Waterways Experiment Station
P. O. Box 631, Vicksburg, Miss. 39180

September 1978

Final Report

D D C

NOV 27 1978

A

REPORT DOCUMENTATION PAGE		READ INSTRUCTIONS BEFORE COMPLETING FORM
1. REPORT NUMBER Technical Report S-78-14	2. GOVT ACCESSION NO.	3. RECIPIENT'S CATALOG NUMBER
4. TITLE (and Subtitle) NON-NORMAL IMPACT AND PENETRATION: ANALYSIS FOR HARD TARGETS AND SMALL ANGLES OF ATTACK		5. TYPE OF REPORT & PERIOD COVERED Final report
		6. PERFORMING ORG. REPORT NUMBER
7. AUTHOR(s) Robert S. Bernard Daniel C. Creighton		8. CONTRACT OR GRANT NUMBER(s)
9. PERFORMING ORGANIZATION NAME AND ADDRESS U. S. Army Engineer Waterways Experiment Station Soils and Pavements Laboratory P. O. Box 631, Vicksburg, Miss. 39180		10. PROGRAM ELEMENT, PROJECT, TASK AREA & WORK UNIT NUMBERS See Block 18
11. CONTROLLING OFFICE NAME AND ADDRESS Defense Nuclear Agency Washington, D. C. 20305		12. REPORT DATE September 1978
		13. NUMBER OF PAGES 77
14. MONITORING AGENCY NAME & ADDRESS(if different from Controlling Office)		15. SECURITY CLASS. (of this report) Unclassified
		15a. DECLASSIFICATION/DOWNGRADING SCHEDULE

16. DISTRIBUTION STATEMENT (of this Report)

Approved for public release; distribution unlimited.

17. DISTRIBUTION STATEMENT (of the abstract entered in Block 20, if different from Report)

18. SUPPLEMENTARY NOTES

This research was sponsored by the Defense Nuclear Agency under Subtask Y99QAXSB211, Work Unit 18, "Penetrator Summary."

19. KEY WORDS (Continue on reverse side if necessary and identify by block number)

Impact	Target vulnerability
Penetration	Targets
Projectile penetration	

20. ABSTRACT (Continue on reverse side if necessary and identify by block number)

A rigid-projectile penetration analysis has been developed for non-normal impact, based on the Cavity Expansion Theory (CET). A modified version of the AVCO penetration code is used to implement the CET analysis, which is intended for hard targets (rock and concrete) and for small angles of attack (less than 10 degrees). Tentative verification has been obtained by comparison with 3-degree reverse ballistic data. More tests are needed for further ─────

(Continued)

20. ABSTRACT (Continued).

verification, but the initial results suggest that the CET analysis can be used by projectile designers to estimate internal and external forces and moments.

Appendix A describes the basic assumptions and results of the CET. Appendix B presents the results of a dynamic structural analysis. Appendix C compares lateral accelerations obtained using the CET and AVCO formulations of the force distribution.

PREFACE

This investigation was sponsored by the Defense Nuclear Agency under Subtask Y99QAXSB211, "Penetration," Work Unit 18, "Penetrator Summary." This study was conducted by personnel of the Soils and Pavements Laboratory (S&PL), U. S. Army Engineer Waterways Experiment Station (WES), during January through December 1977, under the general supervision of Messrs. J. P. Sale and R. G. Ahlvin, Chief and Assistant Chief, S&PL, respectively. Mr. R. S. Bernard formulated the theory and Mr. D. C. Creighton implemented the computer analysis, both under the direct supervision of Dr. J. G. Jackson, Chief of the Soil Dynamics Division (SDD), S&PL. Drs. P. F. Hadala and B. Rohani, SDD, provided technical guidance. Mr. Bernard and Mr. Creighton prepared this report.

COL J. L. Cannon, CE, was Commander and Director of WES during the period of research and report preparation. Mr. F. R. Brown was Technical Director.

CONTENTS

3

CONVERSION FACTORS, U. S. CUSTOMARY TO METRIC (SI)
UNITS OF MEASUREMENT

U. S. customary units of measurement used in this report can be converted to metric (SI) units as follows:

Multiply	By	To Obtain
feet per second	0.3048	metres per second
inches	0.0254	metres
pounds (force) per square inch	6894.757	pascals
inch-pounds	0.1130	newton-metres
pounds (mass)	0.4535924	kilograms
pounds (mass) per cubic foot	16.01846	kilograms per cubic metre
pounds-square inches	0.0002926	kilograms-square metres
slugs per cubic foot	515.50336	kilograms per cubic metre
square inches	0.00064516	square metres

NON-NORMAL IMPACT AND PENETRATION: ANALYSIS FOR

HARD TARGETS AND SMALL ANGLES OF ATTACK

CHAPTER 1

INTRODUCTION

1.1 BACKGROUND

There now exist several techniques that are useful for making pene-
tration predictions, provided the projectile survives the impact and re-
mains stable thereafter. The projectile orientation and motion are usu-
ally assumed normal to the target surface, but perfectly normal impact
seldom occurs in practice. A small angle of attack is ordinarily to be
expected.

The Defense Nuclear Agency (DNA) recently initiated an investiga-
tion of non-normal impact and penetration, with emphasis on small attack
angles (less than 10 degrees[1]). As a part of this effort, DNA asked the
U. S. Army Engineer Waterways Experiment Station (WES) to develop a non-
normal penetration analysis based on the Cavity Expansion Theory (CET).[2]
AVCO Corporation (Reference 1) had previously developed a computer code
for analyzing projectile motion in three dimensions, using an empirical
Differential-Area Force Law (DAFL) to specify the surface loads on the
projectile. The AVCO version of the DAFL code input contains a set of
user-selected empirical parameters describing the target, and it was
felt that the CET analysis might offer a simpler, more rational target
description.

1.2 PURPOSE AND SCOPE

The purpose of this study was to extend the WES CET-based penetra-
tion theory for normal impact (Reference 2) to include non-normal impact.

---

[1] A table of factors for converting U. S. customary units of measurement
to metric (SI) units is presented on page 6.
[2] The Cavity Expansion Theory is discussed in Appendix A.

With the CET analysis in place of AVCO's force distribution, a modified
version of the DAFL code was used to make calculations for comparison
with test data. Sandia Laboratories and AVCO Corporation have each con-
ducted a series of instrumented reverse ballistic tests (RBT's) for DNA
at attack angles between 0 and 10 degrees. Comparison with these tests
shows the CET analysis to be tentatively acceptable as a rigid-body pre-
diction technique for hard targets and small angles of attack.

CHAPTER 2

THEORY

2.1 PROJECTILE MOTION IN TWO DIMENSIONS

Previous CET-based penetration analyses (Reference 2) have addressed only the axial motion of the projectile, obtaining expressions for the total resisting force. The non-normal problem in two dimensions, however, involves three degrees of freedom: one rotational, and two translational (Figure 2.1).

Consider a rigid, deeply buried projectile (no free-surface effects), whose motion lies in the XZ-plane.[1] The rotation is described by the angular velocity $\dot{\theta}$; the translation is described by $\dot{X}$ and $\dot{Z}$, which are the X- and Z-velocity components of the center of gravity (CG).[2,3] For analysis, it is convenient to express the CG velocity in terms of its lateral and axial (x- and z-) components V_x and V_z , respectively:[4]

$$V_x = \dot{X} \cos \theta - \dot{Z} \sin \theta \qquad (2.1)$$

$$V_z = \dot{X} \sin \theta + \dot{Z} \cos \theta \qquad (2.2)$$

For purely axial motion ($V_x = 0$, $\dot{\theta} = 0$), the force distribution on the projectile is symmetric, and the net force is in the z-direction. The introduction of rotation ($\dot{\theta} \neq 0$) and lateral motion ($V_x \neq 0$) destroys this symmetry, and simplifying assumptions are necessary in order to calculate the resulting (asymmetric) force distribution.

Whenever the lateral and rotational velocities are small

---

[1] The XZ-coordinate system is fixed in the target (Figure 2.1).
[2] A dot above any quantity indicates differentiation with respect to time.
[3] For convenience, symbols and abbreviations used in this report are listed and defined in the Notation, Appendix D.
[4] The xz-coordinate system is fixed on the projectile axis, with its origin at the CG (Figure 2.1).

$(V_x \ll V_z$, $L\dot{\theta} \ll V_z$ where L is projectile length), their contributions to the force distribution are assumed to be independent of the axial motion. Thus, defining the angle of attack as

$$\alpha = \tan^{-1} \left(\frac{V_x}{V_z} \right) \tag{2.3}$$

the force contributions due to axial, lateral, and rotational motion can be defined separately when $\tan \alpha \ll 1$ and $\dot{\theta} \ll V_z/L$.[5]

Initially it is assumed that the entire projectile is in contact with the target. This assumption will later be modified when the effect of wake separation is investigated. Whether or not there is contact at a given point, the following assumption will remain in effect throughout the analysis: When any point on the projectile surface moves away from the adjacent target material, the stress at that point is zero.

2.2 FORCE DISTRIBUTION DUE TO AXIAL MOTION

For purely axial motion, the axial resisting force can be calculated by assuming that only normal stresses act on the projectile surface.[6] Assuming further that the axial force is unchanged for small attack angles, the following equation is used to approximate the compressive normal stress due to axial motion only:[7]

$$\sigma_a = \sigma_s + V_z \sqrt{\rho \sigma_s (1 + \sin \eta)} \tag{2.4}$$

where

---

[5] The $\dot{\theta}$ criterion will always be satisfied for stable projectiles when $\tan \alpha \ll 1$.

[6] The analysis in Reference 2 contains both normal and tangential stresses. For hard targets such as rock and concrete, however, the calculated tangential stresses are small enough to be ignored.

[7] Equation 2.4 is an assumed stress distribution that produces an approximation for the net axial force when integrated over the projectile surface.

σ_s = radial compressive stress at the surface of a slowly expanding spherical cavity in the target material (Appendix A)

ρ = target mass density

$\tan \eta$ = slope of projectile surface at a given point, with respect to axis of symmetry[8] (Figure 2.1)

The x- and z-components of σ_a are, respectively,

$$\sigma_x' = \sigma_a \cos \eta \cos \psi \tag{2.5}$$

$$\sigma_z' = \sigma_a \sin \eta \tag{2.6}$$

where ψ is the azimuthal angle (Figure 2.2). For purely axial motion, with complete contact between target and projectile, only Equation 2.6 contributes to the net resisting force (no net lateral force). Otherwise there _is_ a net lateral contribution from Equation 2.5.

2.3 FORCE DISTRIBUTION DUE TO LATERAL MOTION

For small atta:k angles, the resisting force due to lateral motion is presumed to be unaffected by the axial motion. In this sense, the lateral motion can be regarded as a "separate" penetration problem, and it is assumed that the lateral motion produces only lateral resistance.

Dropping the nose shape factor $(1 + \sin \eta)$ and replacing V_z with V_x , the expressions for the x- and z-components of the compressive stress due to lateral motion are assumed to be[9]

$$\sigma_x'' = \begin{cases} (\sigma_s + V_x \sqrt{\rho \sigma_s}) \cos \eta \cos \psi \,, & V_x > 0 \\ (\sigma_s - V_x \sqrt{\rho \sigma_s}) \cos \eta \cos \psi \,, & V_x < 0 \end{cases} \tag{2.7}$$

---

[8] The quantity $1 + \sin \eta$, which appears in Equation 2.4, is an empirical "nose shape" factor, introduced to produce a gradual increase in axial resistance with increasing nose bluntness $(\sin \eta)$.

[9] Equations 2.7 and 2.8 are analogous to Equations 2.5 and 2.6. The nose shape factor is eliminated in the lateral stress because all projectiles of interest have circular cross sections.

11

$$\sigma_z'' = 0 \tag{2.8}$$

Wherever $V_x \cos \psi < 0$, the lateral translation of that point is _away_ from the adjacent target material, and so $\sigma_x'' \equiv 0$ for that point on the projectile.

2.4 FORCE DISTRIBUTION DUE TO ROTATION

Assuming that the lateral velocity due to pure rotation $z\dot\theta$ merely adds an additional velocity term to Equation 2.7, the x- and z-components of the compressive stress due to rotation are

$$\sigma_x''' = z\dot\theta \sqrt{\rho\sigma_s} \cos \eta \cos \psi \tag{2.9}$$

$$\sigma_z''' = 0 \tag{2.10}$$

Wherever $z\dot\theta \cos \psi < 0$, the rotation is _away_ from the adjacent target material, and so $\sigma_x''' \equiv 0$ for that point on the projectile.

2.5 COMPOSITE FORCE DISTRIBUTION

Equations 2.5 through 2.10 can now be combined to obtain the composite axial and lateral force distributions on the projectile. The net axial stress is

$$\sigma_z = \sigma_z' + \sigma_z'' + \sigma_z''' = \sigma_z' \tag{2.11}$$

The net lateral stress is

$$\sigma_x = \sigma_x' + \sigma_x'' + \sigma_x''' \tag{2.12}$$

The lateral and axial force components (Figure 2.2) acting on any surface element dA are, respectively,

$$dF_x = -\sigma_x \, dA \tag{2.13}$$

12

$$dF_z = -\sigma_z \, dA \qquad (2.14)$$

where dA is the differential surface area. The lateral and axial
force components acting on the entire projectile are then

$$F_x = -\int_A \sigma_x \, dA \qquad (2.15)$$

$$F_z = -\int_A \sigma_z \, dA \qquad (2.16)$$

where A represents the entire projectile surface. The translational
equations of motion are

$$M\ddot{X} = F_x \cos\theta + F_z \sin\theta \qquad (2.17)$$

$$M\ddot{Z} = -F_x \sin\theta + F_z \cos\theta \qquad (2.18)$$

where M is the projectile mass and $\ddot{X}$ and $\ddot{Z}$ are the components of
acceleration in the X- and Z-directions, respectively. The projectile
is assumed rigid, and the rotational equation of motion is

$$I_{CG}\ddot{\theta} = \int_A z \, dF_x - \int_A x \, dF_z \qquad (2.19)$$

where I_{CG} is the mass moment of inertia about the CG, and $\ddot{\theta}$ is
the angular acceleration. The right-hand side of Equation 2.19 is the
total moment exerted on the projectile about its CG.

2.6 WAKE SEPARATION AND REATTACHMENT

It is likely that some parts of the projectile lose contact with
the target during penetration. Part of the nose must remain in contact,
but separation can occur anywhere, especially on the aftbody. While a
precise analysis of the separation mechanism itself is unmanageable, it
is still possible to assess the gross effect of a specified amount of
separation upon the projectile.

13

Consider a projectile with no rotational or lateral velocity ($\dot{\theta} = 0$, $V_x = 0$). Separation is thought to occur near the base of the nose (Figure 2.3), with reattachment somewhere on the aftbody (if anywhere). The separation and reattachment points probably change with velocity, and the width of the separation gap may vary with position. This behavior is simplified and idealized (Figure 2.4) in the following assumptions:

1. The entire nose is in contact with the target.

2. The width of the separation gap δ between aftbody and target is directly proportional to the local aftbody radius r .

Assumption 1 is reasonable for long projectiles, for which the nose represents only a fraction of the total surface area. According to Assumption 2, a cavity exists in the target aft of the nose (Figure 2.4), such that δ/r remains constant. These assumptions have no effect whenever $V_x = 0$ and $\dot{\theta} = 0$. However, if $V_x \neq 0$ or $\dot{\theta} \neq 0$, then there is a distribution of local lateral velocity

$$v_x = V_x + z\dot{\theta} \qquad (2.20)$$

and part of the aftbody surface may collide with the cavity wall (which is regarded as fixed). Reattachment is defined as any collision between the aftbody and the cavity wall.

The problem is still complicated because the cavity wall will not be straight if $V_x \neq 0$ or $\dot{\theta} \neq 0$. Instead, it will be a curved cylindrical surface, mapping out the trajectory of the nose base. Additional simplification is necessary if the analysis is to be tractable.

Consider the two views of the idealized wake separation shown in Figure 2.4. Suppose that the cavity is almost straight between points 1 and 2, but that point 1 (on the projectile) is moving toward the cavity wall. The simplified reattachment criterion is as follows: if point 1 can collide with the cavity wall before going past point 2, then point 1 is assumed to be already in contact with the cavity wall. Thus, the condition required for contact is

14

$$-\frac{\delta}{v_x} < \frac{s}{V_z} \qquad (2.21)$$

where s is the axial distance between the point in question and the base of the nose. At arbitrary points on the aftbody (such as point 3), one of the following conditions is required for contact:

$$\frac{\sqrt{r^2 \cos^2 \psi + 2r\delta + \delta^2} - r \cos \psi}{v_x} < \frac{s}{V_z} , \qquad -\frac{\pi}{2} < \psi < \frac{\pi}{2} \quad (2.22)$$

$$\frac{\sqrt{r^2 \cos^2 \psi + 2r\delta + \delta^2} + r \cos \psi}{-v_x} < \frac{s}{V_z} , \qquad \frac{\pi}{2} < \psi < \frac{3\pi}{2} \quad (2.23)$$

Wherever this condition is satisfied (on the aftbody), the stress is defined by Equations 2.11 and 2.12; otherwise, the stress is set equal to zero (no contact).

2.7 INTERNAL FORCES AND MOMENTS IN A RIGID PROJECTILE

The external forces and moments create internal forces and moments within the rigid projectile itself. According to D'Alambert's principle, the x- and z-components of the internal force at any point z on the axis of symmetry are, respectively,

$$f_x(z) = \int_{\xi=z_n}^{\xi=z} [dF_x(\xi) - \dot{v}_x \, dM(\xi)] \qquad (2.24)$$

$$f_z(z) = \int_{\xi=z_n}^{\xi=z} [dF_z(\xi) - \dot{v}_z \, dM(\xi)] \qquad (2.25)$$

where z_n is the z-coordinate of the nose tip, the differential function dM(z) represents the point distribution of mass along the

15

projectile axis $(x = 0)$, and ξ is a variable of integration. The differential force-components, $dF_x(z)$ and $dF_z(z)$, are given by Equations 2.13 and 2.14. The local lateral and axial accelerations are given by

$$\dot{v}_x = \frac{d}{dt}\, v_x = \frac{d}{dt}\, V_x + z\ddot{\theta} \tag{2.26}$$

$$\dot{v}_z = \frac{d}{dt}\, v_z = \frac{d}{dt}\, V_z - z\dot{\theta}^2 - x\ddot{\theta} \tag{2.27}$$

The internal (bending) moment at z is

$$\Gamma(z) = \int_{\xi=z_n}^{\xi=z} (z_n - \xi)\, dF_x(\xi) + \int_{x=-r}^{x=+r} x\, dF_z(x,z)$$

$$- \int_{\xi=z_n}^{\xi=z} \int_{x=-r}^{x=+r} [(z_n - \xi)\, \dot{v}_x - x\dot{v}_z]\, dM(x,\xi) \tag{2.28}$$

The differential functions $dM(x,z)$ and $dF_z(x,z)$ represent the distributions of mass and external axial force, respectively, throughout the projectile.

2.8 MODIFIED AVCO COMPUTER CODE

The equations for the x- and z-components of stress (Equations 2.11 and 2.12) have been installed in a modified version of the AVCO DAFL code, replacing the AVCO definitions of the same quantities. Algorithms have also been added for calculating internal force (Equations 2.24 and 2.25) and bending moment (Equation 2.28) in a rigid projectile. Figure 2.5 shows a block diagram for calculations using the CET analysis and the modified DAFL code.

2.9 RESTRICTION TO HARD TARGETS AND SMALL ANGLES OF ATTACK

The theory in Sections 2.1 through 2.7 is intended only for hard targets such as rock and concrete. Furthermore, since the analysis uses purely axial motion as a point of departure from normal impact, calculations should be restricted to small angles of attack ($\alpha \leq 10$ degrees), for which the projectile motion is predominantly axial.

NOTE X-Z COORDINATE SYSTEM IS
      FIXED IN THE TARGET

      x-z COORDINATE SYSTEM IS
      FIXED ON PROJECTILE
      AXIS, WITH ORIGIN AT CG
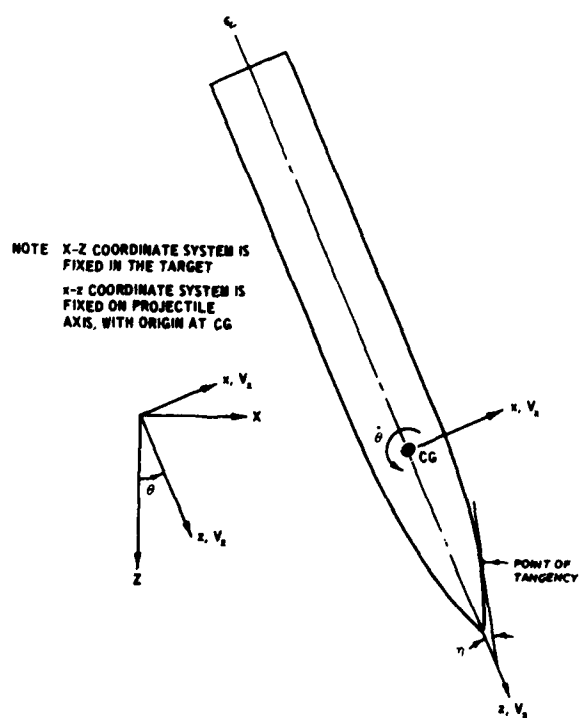
Figure 2.1   Projectile motion in two dimensions.

18
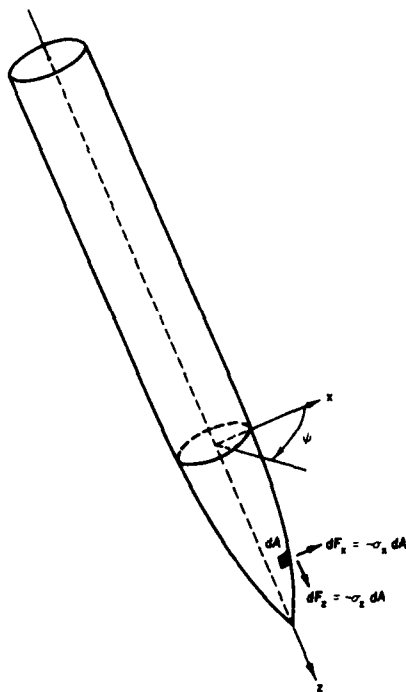
Figure 2.2 Three-dimensional view of projectile.
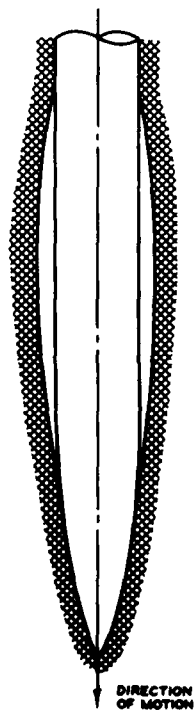
Figure 2.3 Wake separation and reattachment for
purely axial motion.
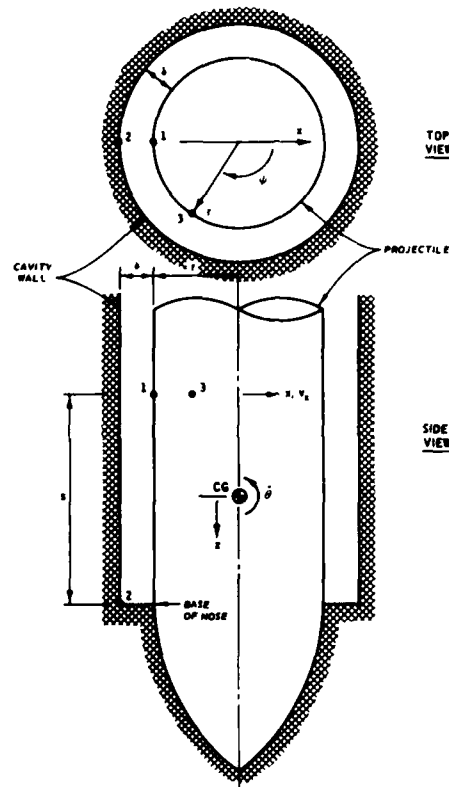
Figure 2.4   Idealized wake separation.
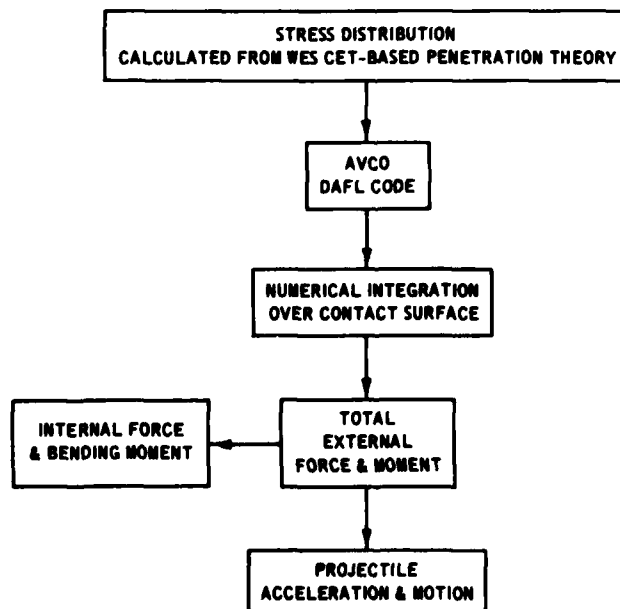
Figure 2.5   Block diagram for non-normal impact-and-penetration
calculations using CET analysis and AVCO DAFL code.

20

CHAPTER 3

CALCULATIONS AND TEST DATA

3.1 AVAILABILITY OF NON-NORMAL TEST DATA

Direct measurements of the lateral forces incurred by a projectile during non-normal impact and penetration are scarce. In fact, with the exception of tests recently conducted by Sandia Laboratories (References 3 and 4) and AVCO Corporation[1] (References 5 and 6), lateral force-related data are virtually nonexistent. These tests seem to offer the only benchmarks for checking the theory formulated in Chapter 2, but the available data are too few to establish the general credibility of the theory. More tests are needed under different impact conditions, and the test results that do exist are sufficient only for tentative verification.

3.2 LIMITATIONS AND SIMPLIFICATIONS IN THE CET ANALYSIS

The CET analysis is intended for calculations in which the initial angle of attack is less than 10 degrees. The primary assumption is that, for small attack angles, the lateral resisting force can be found by linear superposition of axial, lateral, and rotational effects.

It will be shown that aftbody wake separation has little effect in the calculations if the assumed separation gap width δ is small compared to the local aftbody radius r . For hard targets it is likely that the projectile-target separation is small; thus the comparison of calculations and test data will be made on the assumption that $\delta/r \approx 0$. The parametric effect of varying δ/r in the calculations will be shown separately.

The quantity σ_s , which appears in Chapter 2, is discussed in

---

[1] Personal communication dated 10 May 1977 from P. J. Grady, AVCO Corporation, Wilmington, Mass., to MAJ D. Spangler, Defense Nuclear Agency, Washington, D. C.

Appendix A. Defined in terms of the target shear strength, σ_s links the CET to the penetration theory. For calculations in hard materials (Reference 2), it has been found acceptable to assume that the target obeys the von Mises failure condition. The strength parameters (Appendix A) then become

$$\phi_1 = \phi_2 = 0 \qquad (3.1)$$

$$c_1 = c_2 = \frac{1}{2} Y \qquad (3.2)$$

where Y is the unconfined compressive strength. The expression for σ_s reduces to

$$\sigma_s = \frac{2}{3} Y(1 + \ln I_1) \qquad (3.3)$$

where I_1 is the rigidity index, given by

$$I_1 \approx \frac{2E}{3Y} \qquad (3.4)$$

and E is Young's modulus for the target.

3.3 SANDIA REVERSE BALLISTIC TESTS

3.3.1 Test Description

Sandia Laboratories has conducted a series of RBT's for both normal and non-normal impact. In each of the experiments, a sandstone target[2] was mounted on a rocket sled and accelerated to a velocity of about 1500 ft/s before striking a stationary 1.9-inch-diameter projectile. Two of the tests were conducted at attack angles of 3 degrees; the impact conditions, projectile parameters, and sandstone properties for these tests are shown in Figure 3.1.

The projectiles were instrumented with strain gages and with lateral

---

[2] The targets were hexagonal prisms, 45 inches across and 30 inches deep (in the direction of motion).

and axial accelerometers (Figure 3.2), and data were recorded for the first body length of penetration. The outputs of the accelerometers (at stations F and R) and the strain gage (at station S)[3] can be compared directly with the predictions of the CET analysis.

3.3.2 Accelerometer Data

Figures 3.3 and 3.4 show comparisons of the calculated and measured acceleration records for the forward accelerometer location (station F). The axial deceleration calculation (Figure 3.3) reproduces the experimental results about as accurately as can be expected for a rigid-body calculation. The lateral acceleration records for this station (Figure 3.4) are more difficult to appraise. The CET calculation reproduces the maximum acceleration levels, but not the instantaneous details.

Figures 3.5 and 3.6 show the calculated and measured acceleration records for the rear accelerometers (station R). Again, the axial deceleration calculation is in reasonable agreement with the experimental results (Figure 3.5). Figure 3.6, however, offers a more dramatic comparison of lateral acceleration records than does Figure 3.4. The experimental acceleration records show about the same magnitude and duration as the calculated results, but the peaks occur later than the calculated results. This delay is apparently caused by nonrigid projectile response to the rapidly varying applied loads (Appendix B).

3.3.3 Strain Gage Data

In the CET analysis it is assumed that the projectile is perfectly rigid, but actually strains are produced in the projectile by the internal force f_z and bending moment Γ. In the plane of motion, the expression for the maximum axial strain ε_a on either side of the projectile is

$$\varepsilon_a = \frac{f_z}{E_p A_s} \pm \frac{r_s \Gamma}{E_p I_s} \qquad (3.5)$$

where

E_p = Young's modulus for projectile

---

[3] There were strain gages at several locations, but the one nearest the CG has been chosen for discussion.

23

A_s = area of projectile cross section S

r_s = projectile radius at section S

I_s = area moment of inertia of projectile cross section S

If ϵ_a is small and f_z and Γ are slowly varying functions of time, then Equation 3.5 is an exact formula for the strain gage output.

Figure 3.7 shows a comparison of the calculated and measured axial strains for strain gage S (Figure 3.1). The calculated and experimental strain levels are about the same, but the experimental results are delayed, as were the lateral acceleration data. Again, the delay seems to be caused by the rapidly varying applied loads (Appendix B).

3.4 PARAMETER STUDY

The real test of the CET analysis lies not in the prediction of individual test results, but in the prediction of the results (or trends) observed in many tests. The data required for such a verification are as yet unavailable, but it is still worthwhile to investigate the importance of different parameters in the calculations themselves. Accordingly, a brief study has been made in which the attack angle, the impact velocity, the target strength, and the wake separation were varied. The Sandia test conditions were used as a baseline, and the projectile parameters (Figure 3.1) were held fixed.

3.4.1 Calculated Effect of Attack Angle

Figure 3.8 shows the lateral acceleration of the projectile CG for different initial values of the attack angle. Beyond the point of nose embedment (0.2 ms), there is a marked difference in acceleration level for attack angles of 1, 3, and 5 degrees. The same is true of the bending moment (Figure 3.9).

An increase in the initial attack angle clearly raises the magnitudes of the lateral acceleration and the bending moment. This rise is a direct consequence of Equations 2.5, 2.7, and 2.9 in Chapter 2.[4] The

---

[4] Appendix C presents a comparison of lateral accelerations obtained with the WES and the AVCO formulations of the force distribution.

rate of rise, however, awaits experimental data for verification. If future tests generally show a stronger-than-predicted increase in acceleration and bending moment with increasing attack angle, then the velocity terms in the lateral stress equations will need to be enlarged, with the σ_s terms reduced.

3.4.2 Calculated Effect of Impact Velocity

Aside from decreasing the lateral acceleration and the bending moment, a reduction of the impact velocity lengthens the time required for penetration, and vice versa (Figures 3.10 and 3.11). From the calculations, it also appears that a given change in the impact velocity has a stronger effect than the same relative change in the angle of attack. In this case a factor of 2 increase in the impact velocity produces about the same increase in the lateral load as a factor of 5 change in the attack angle.

3.4.3 Calculated Effect of Target Strength

Inspection of Equations 2.5, 2.7, 2.9, and 3.3 reveals that the loads on the projectile must exhibit a target-strength dependence that falls somewhere between linear and square root. For an impact velocity of 1500 ft/s and an attack angle of 3 degrees, the lateral acceleration and the bending moment are roughly proportional to the square root of the strength, as can be seen from Figures 3.12 and 3.13. At much lower velocities, the dependence will be more nearly linear.

3.4.4 Calculated Effect of Wake Separation

The analysis of wake separation in Chapter 2 is insufficient for predicting separation. It is, however, adequate for assessing the consequences of a specified amount of separation. Thus, by varying the ratio δ/r , it is possible to find out the degree to which separation (and reattachment) may influence the loads on the projectile.

The value $\delta/r = 0$ represents no initial wake separation, but parts of the projectile may rotate away from the target, thereby losing contact. The value $\delta/r = 1$ represents an unreasonably large amount of

separation (see Figure 2.4). For rock and concrete, ratios on the order of $\delta/r \approx 0.1$ seem reasonable.

Figures 3.14 and 3.15 show the results of calculations made with different values of δ/r. The variation of δ/r has little influence on the maximum lateral acceleration, affecting only the pulse duration. The bending moment is more strongly affected, especially by the larger values of δ/r. Nevertheless, the bending moment and the lateral acceleration are essentially unchanged when δ/r is increased from 0.0 to 0.1. According to the calculations, a great deal of separation ($\delta/r \geq 0.5$) is required to produce a significant change in the bending moment.

3.5 AVCO REVERSE BALLISTIC TESTS

The Sandia RBT's offer perhaps the best non-normal penetration data on record, since the projectiles were fully instrumented and the targets were large enough to delay edge effects for a whole body length of penetration. However, the only nonzero angle of attack used was 3 degrees. At least one more value is needed to establish or verify a relation between the projectile loads and the attack angle for a specified target. AVCO Corporation has conducted RBT's in concrete for angles of 2, 5, and 10 degrees.

3.5.1 Test Description

The projectile parameters, target properties, and impact conditions for the AVCO tests are given in Figures 3.16 and 3.17. A 5-degree angle was tested at 1050 ft/s, and all angles were tested at 1500 ft/s. All the projectiles were instrumented with strain gages,[5] but only the 1050-ft/s projectile was instrumented with accelerometers.

In each of the tests a concrete cylinder 15 inches across and 9 inches deep was fired from a gun, striking a stationary 3-inch-diameter projectile. Due to the size of the target and the sonic speed ($\approx$8000 ft/s) in the concrete, the tests were free of edge effects for no more than 0.2 ms.[6]

---

[5] Only the strain gage S, shown in Figures 3.18 and 3.19, has been chosen for discussion.

[6] In the Sandia tests, edge effects were absent for about 1 ms, or 18 inches of penetration.

26

3.5.2 Accelerometer Data for 1050-ft/s Test

Figure 3.20 shows a comparison of the axial deceleration data with the CET results for the 1050-ft/s test. Except for the peaks in the test record, the calculation overshoots the data by at least a factor of 2 after the first 0.4 ms. Thus, the penetration resistance of the concrete is either (1) less than indicated by the strength or (2) affected by the target dimensions.

It is likely that the low penetration resistance is the result of a low ratio of target diameter to projectile diameter (5 in this case). In the Sandia tests, this ratio was 30, and the calculated deceleration matched the test data. The larger the ratio, the better the target simulates a half-space. (An infinite ratio is assumed in the calculations.)

Figure 3.21 shows a comparison of the calculated and measured lateral accelerations for the forward accelerometer.[7] The sharp spikes in the <u>calculated</u> results are due to the integration scheme used in the code,[8] and there is so much oscillation in the test data that the comparison is difficult to appraise.

3.5.3 Strain Gage Data for 1050-ft/s Test

The measured strains for the 1050-ft/s test (Figure 3.22) are much lower than the calculated strains for the same reason that the accelerometer data (Figure 3.21) were low. Furthermore, the onset of strain is delayed, as in the Sandia tests. After the delay, the initial rise in the measured strain is comparable with the calculated strain, but the rise rate drops after about 0.2 ms, probably due to edge effects.

3.5.4 Strain Gage Data for 1500-ft/s Tests

Measured and calculated strains for the 1500-ft/s tests are shown in Figures 3.23 through 3.25. Again, the onset of the measured strain

---

[7] The rear lateral accelerometer failed to operate.
[8] The same is true for all calculated results shown hereafter.

is delayed, and the observed strain levels are much lower than calculated. The discrepancy between the data and the CET analysis decreases with increasing attack angle, but this decrease does not necessarily mean that the predictions are more accurate for higher attack angles in general. Figure 3.26 indicates that the calculated maximum strain is a linear function of the attack angle, while the measured maximum strain is non-linear.[9] The nonlinearity may be due to edge effects, in which case the comparison made in Figure 3.26 is inappropriate. Overprediction of the strain is to be expected for small targets; but if future tests for large targets exhibit the same type of nonlinearity, then the CET analysis will require some modification.

---

[9] Individual rapid oscillations are ignored in determining the maximum strain levels from Figures 3.23 through 3.25.

PROJECTILE

0.284-SCALE EARTH PENETRATOR

WEIGHT = 9.48 LB

MAXIMUM DIAMETER = 1.9 IN

MOMENT OF INERTIA = 221.9 LB-IN^2 (ABOUT CG)

NOSE SHAPE: 6.00 CRH OGIVE (BEVELED TIP)

$E_p = 2.8 \times 10^7$ PSI

$I_s = 0.34$ IN^4

$A_s = 1.32$ IN^2

$r_s = 0.85$ IN

NOTE: CRH IS THE OGIVE CALIBER RADIUS

0 _____ 5

SCALE, INCHES

S

LATERAL DIRECTION

1500 FT/S
IMPACT VELOCITY
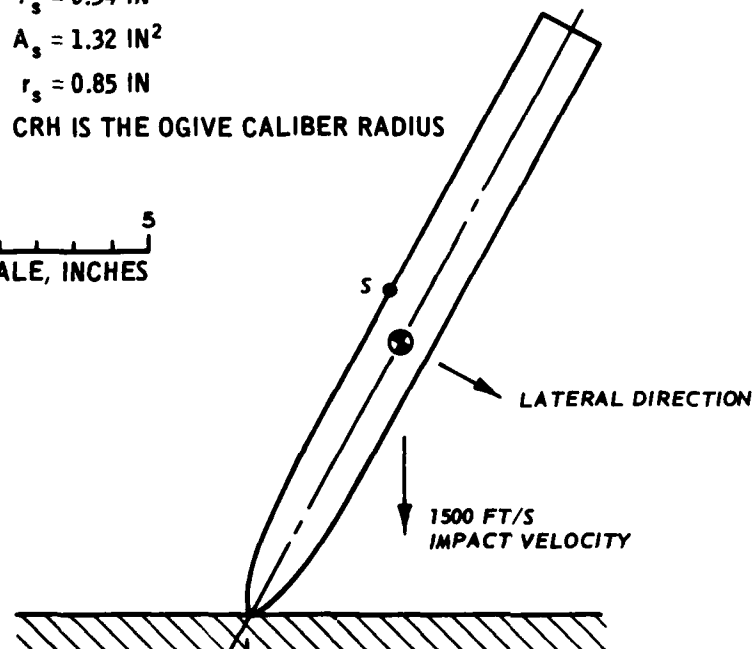
TARGET

SAN YSIDRO SANDSTONE

DENSITY = 130 LB/FT^3

UNCONFINED STRENGTH = 3400 PSI

$\dfrac{\text{SHEAR MODULUS}}{\text{SHEAR STRENGTH}} \approx 95 = $ RIGIDITY INDEX, I_1

3°
ANGLE
OF
ATTACK

AXIAL
DIRECTION

$\phi_1 = \phi_2 = 0$

$c_1 = c_2 = 1700$ PSI

Figure 3.1 Projectile parameters, target properties, and impact
conditions for Sandia RBT's.

29

STATION	LOCATION INCHES	SIGNIFICANCE
B	+4.91	NOSE BASE
CG	0.00	CENTER OF GRAVITY
F	+0.75	FORWARD ACCELEROMETER
R	−8.38	REAR ACCELEROMETER
S	−0.89	STRAIN GAGE
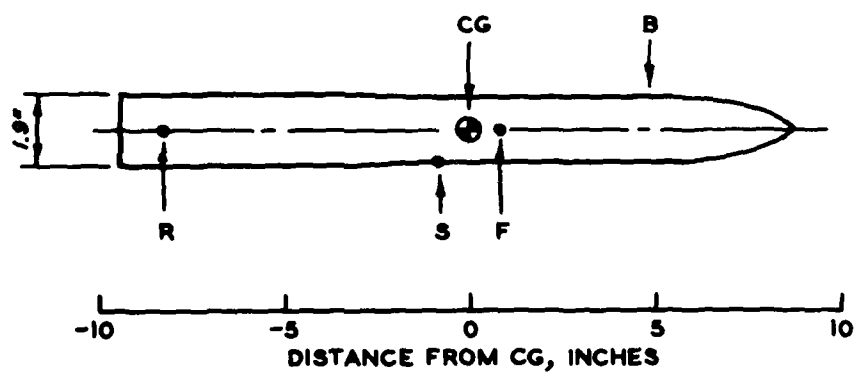
Figure 3.2 Axial location of strain gage and accelerometers for projectile used in Sandia RBT.

30
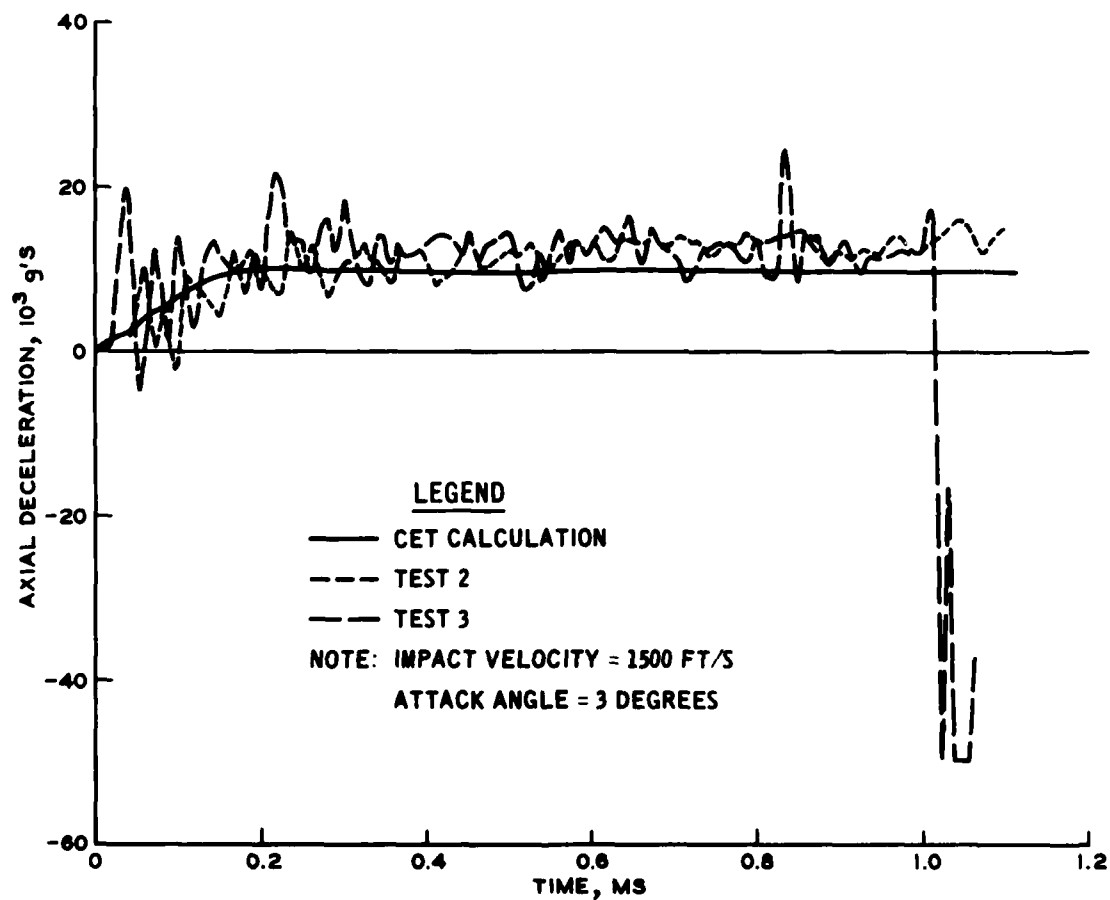
Figure 3.3 Comparison of calculated and measured axial
decelerations for Sandia RBT (forward
accelerometer).
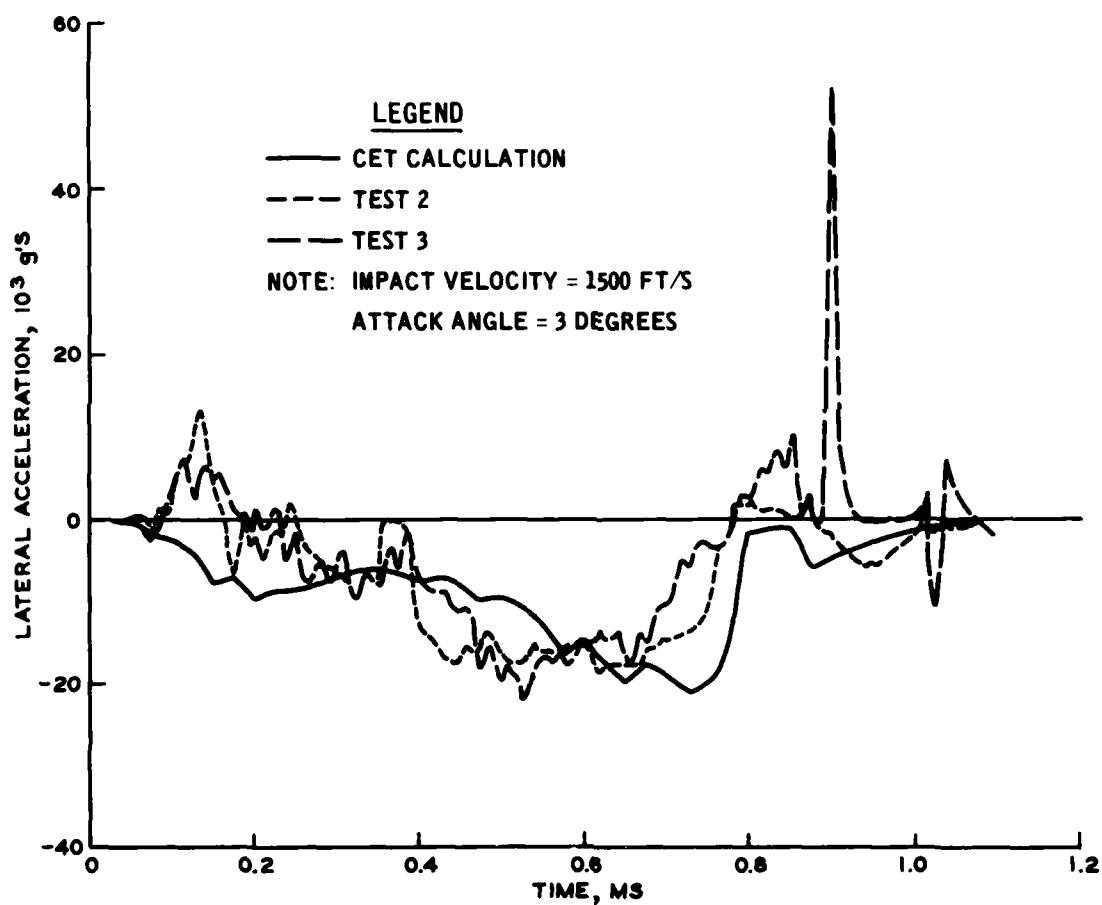
Figure 3.4 Comparison of calculated and measured lateral accelerations for Sandia RBT (forward accelerometer).
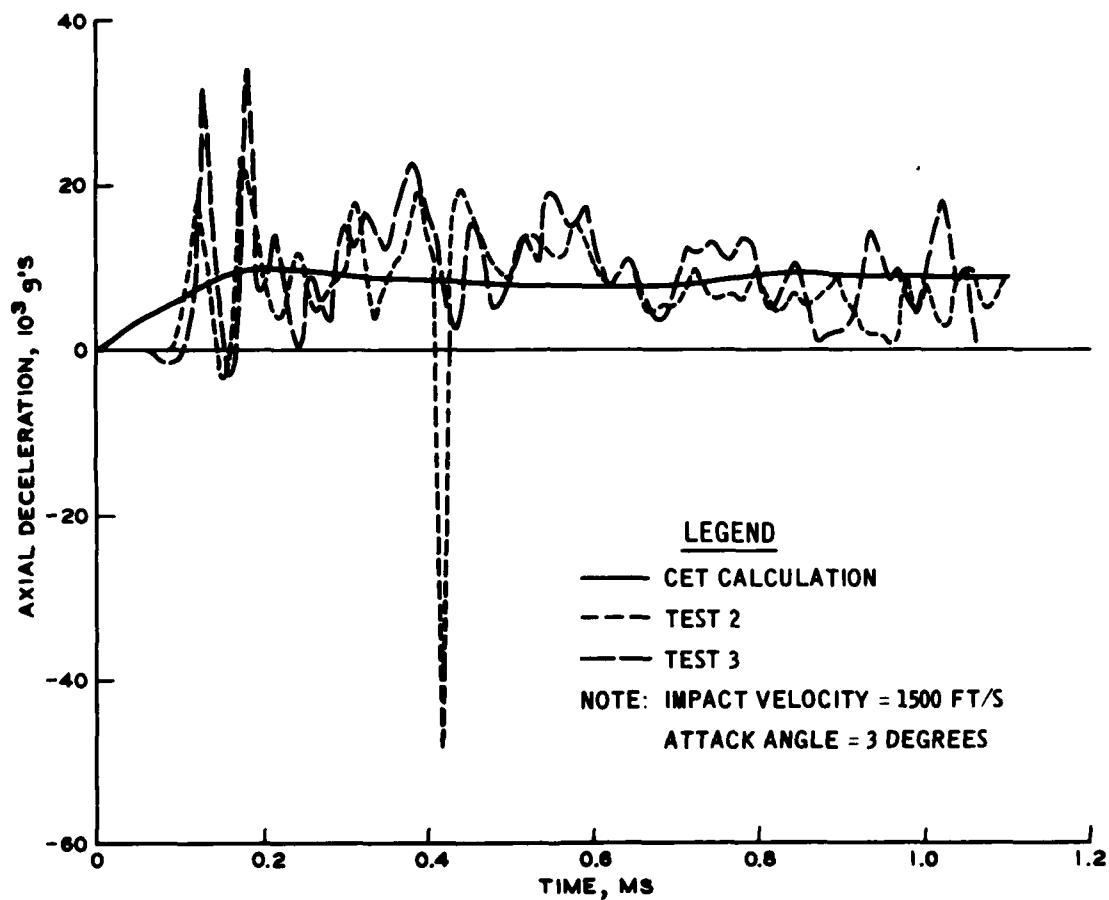
Figure 3.5   Comparison of calculated and measured axial
decelerations for Sandia RBT (rear
accelerometer).
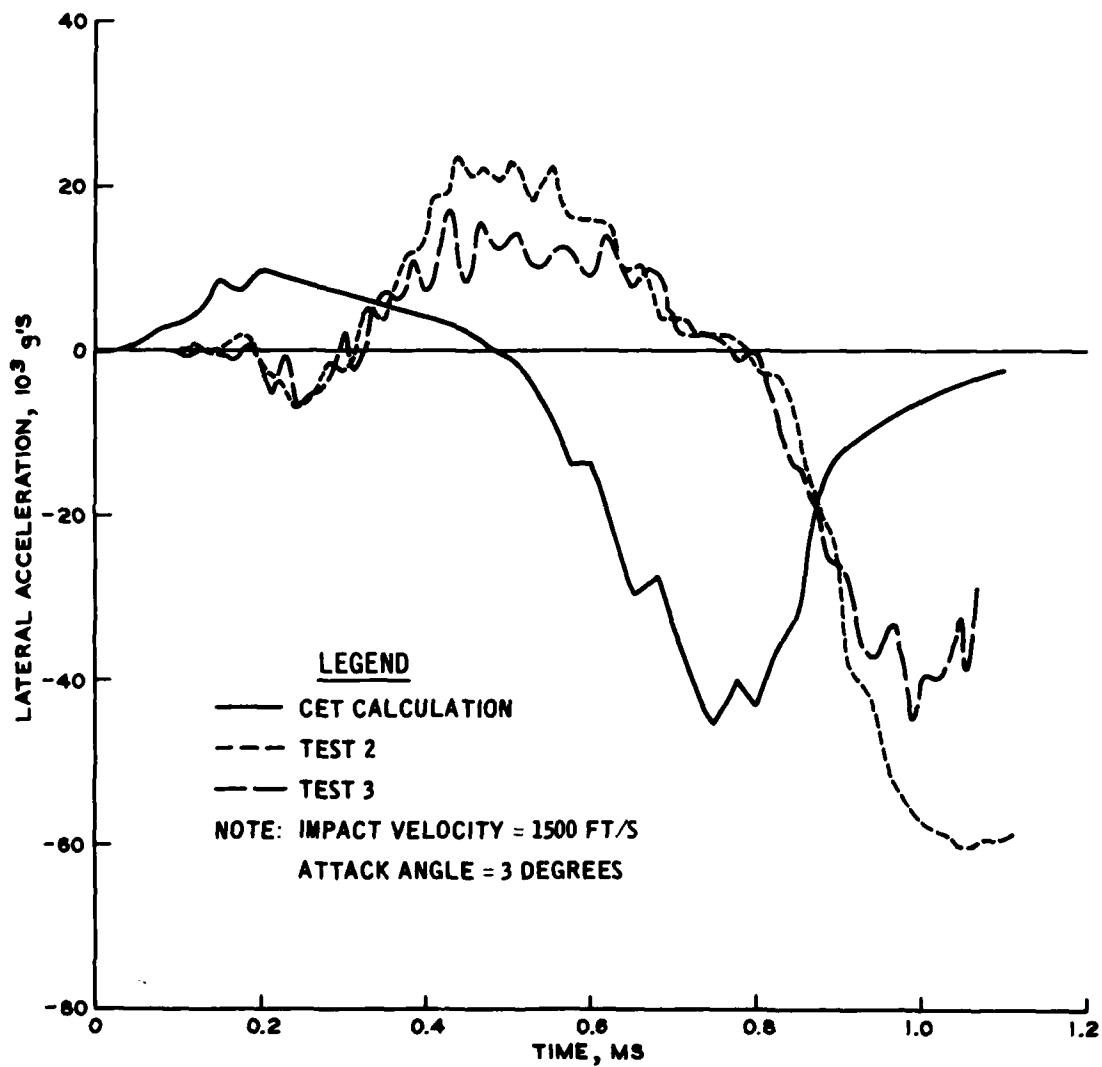
Figure 3.6 Comparison of calculated and measured lateral
accelerations for Sandia RBT (rear
accelerometer).

34
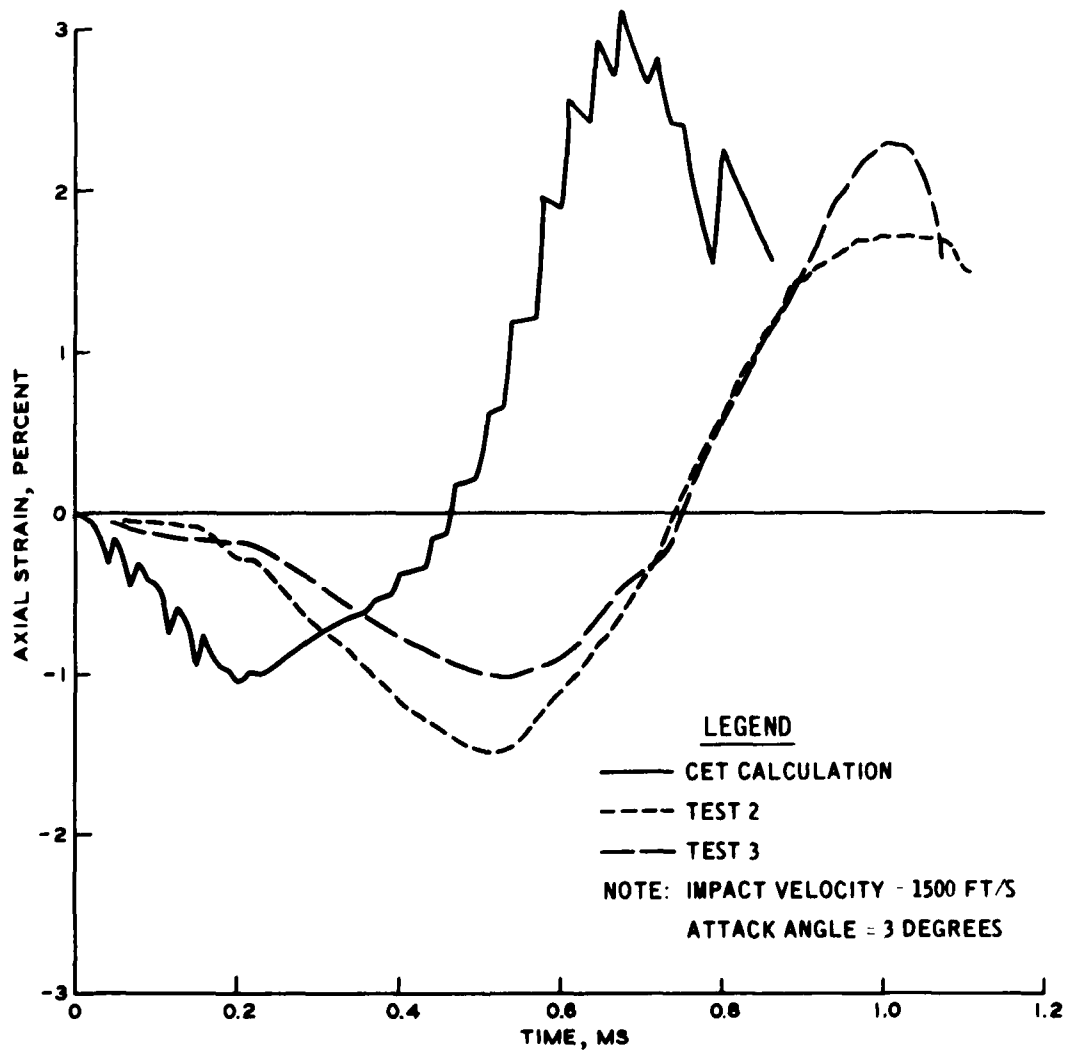
Figure 3.7 Comparison of calculated and measured axial
strains for Sandia RBT, strain gage S.
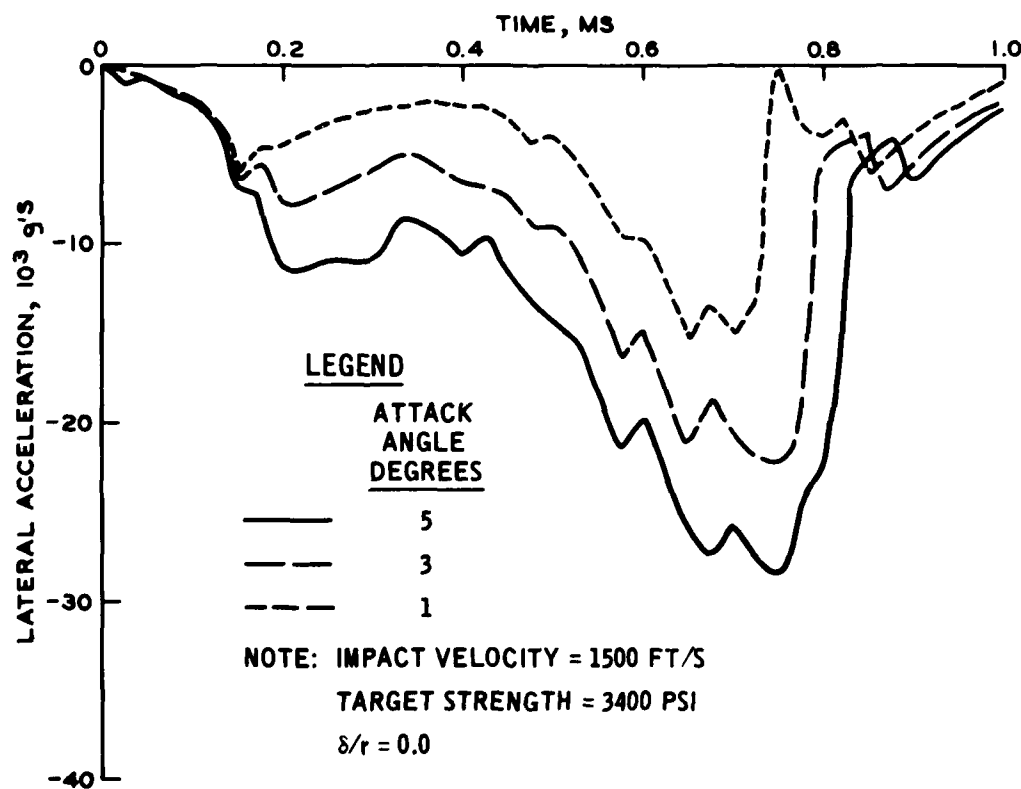
Figure 3.8   Calculated CG lateral acceleration for
             different angles of attack, Sandia RBT.
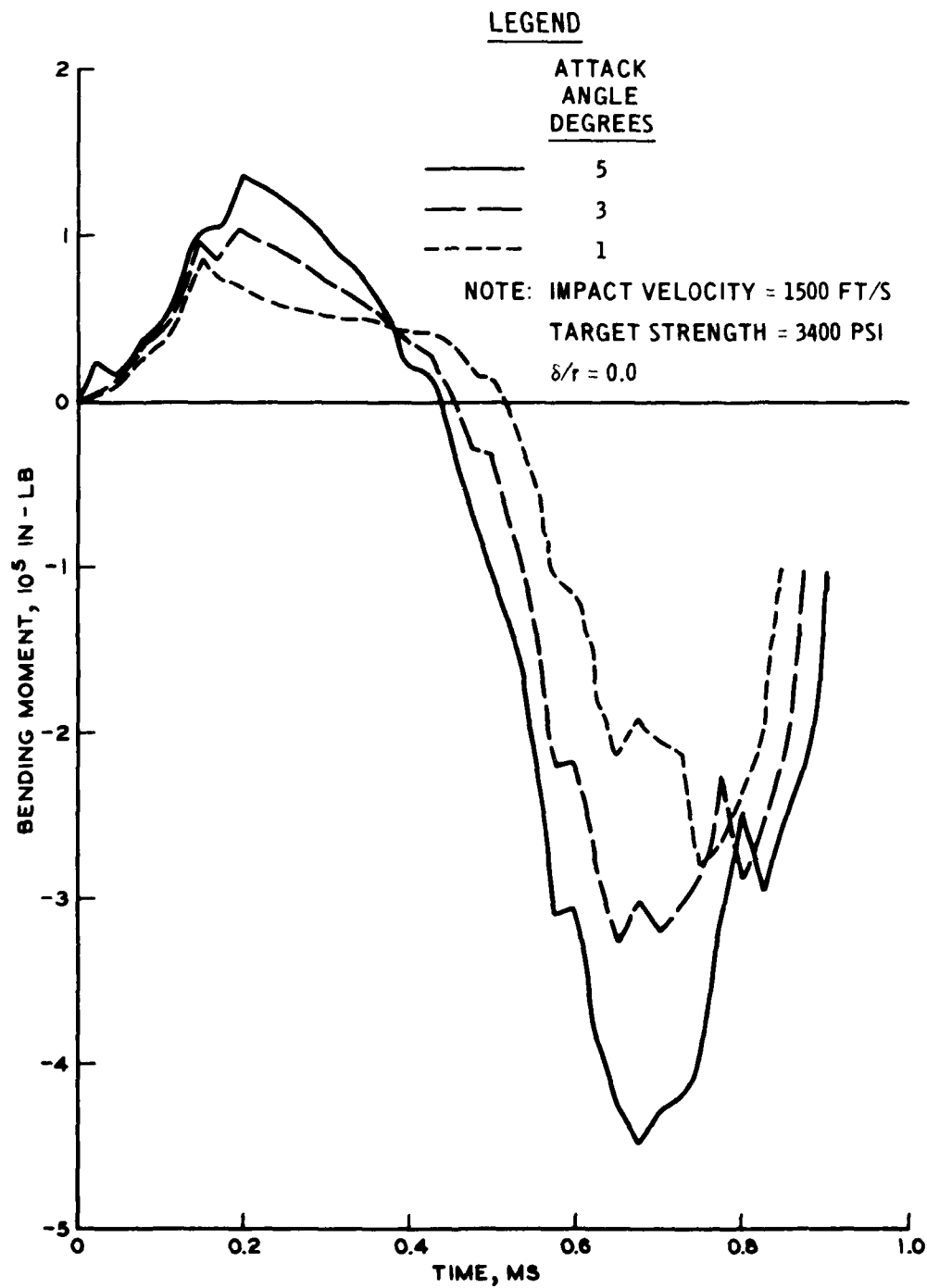
Figure 3.9 Calculated bending moment for different angles of attack, Sandia RBT, section S.

37
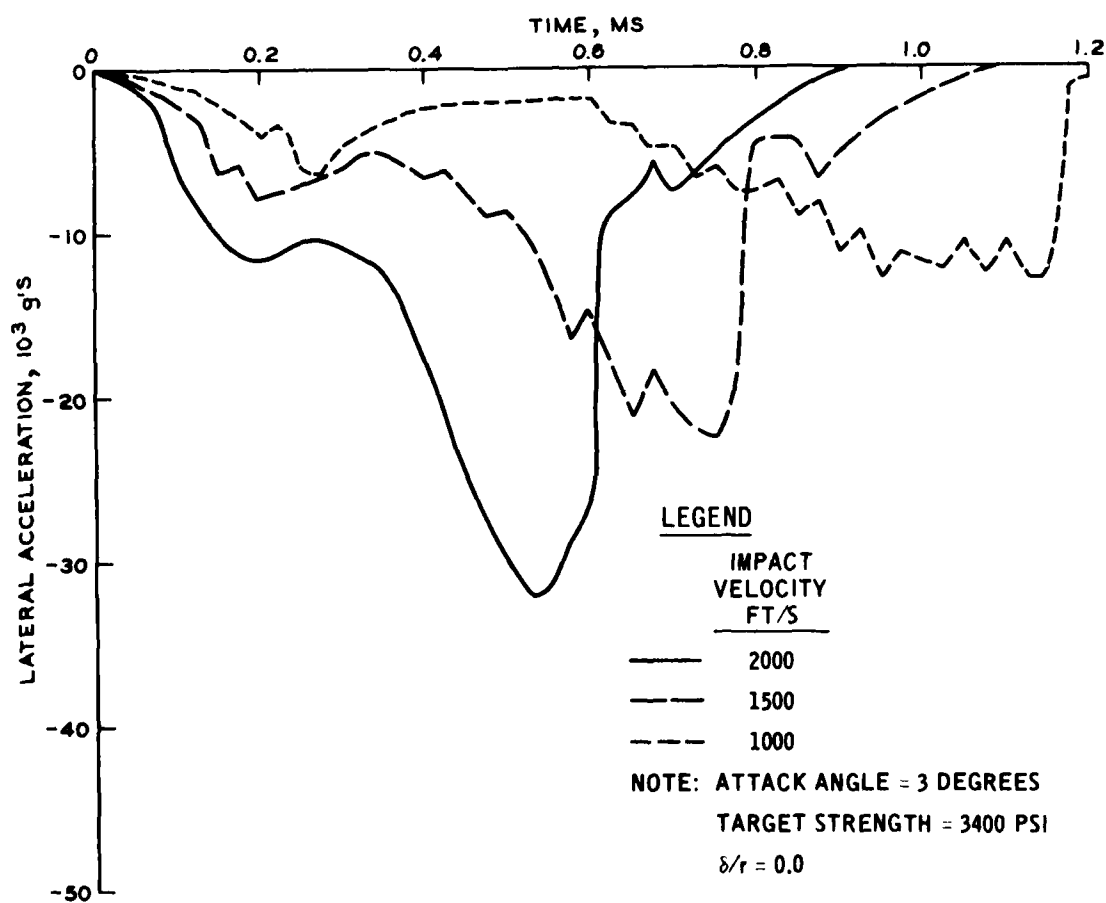
Figure 3.10 Calculated CG lateral acceleration for
different impact velocities, Sandia RBT.
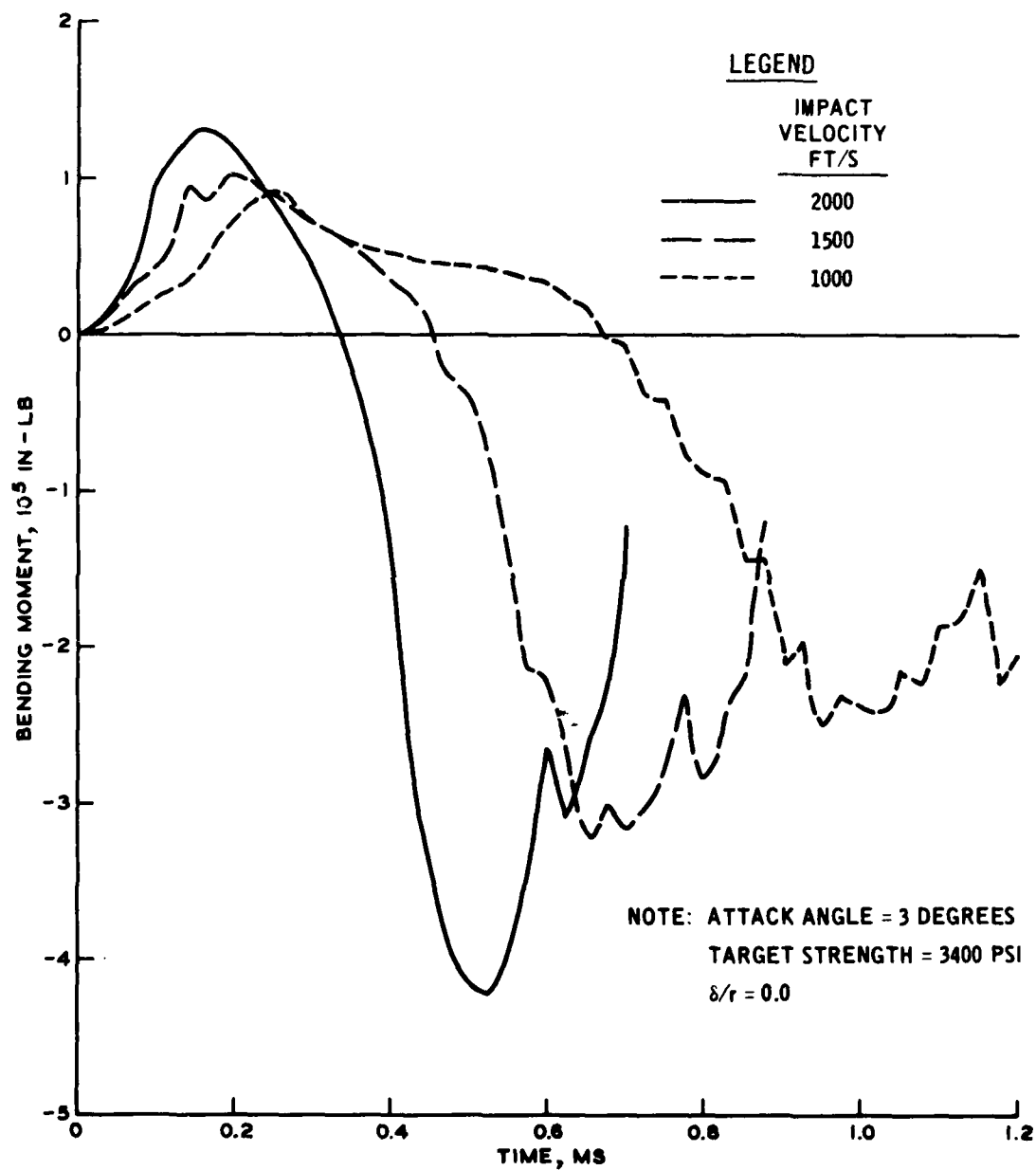
Figure 3.11 Calculated bending moment for different impact velocities, Sandia RBT, section S.
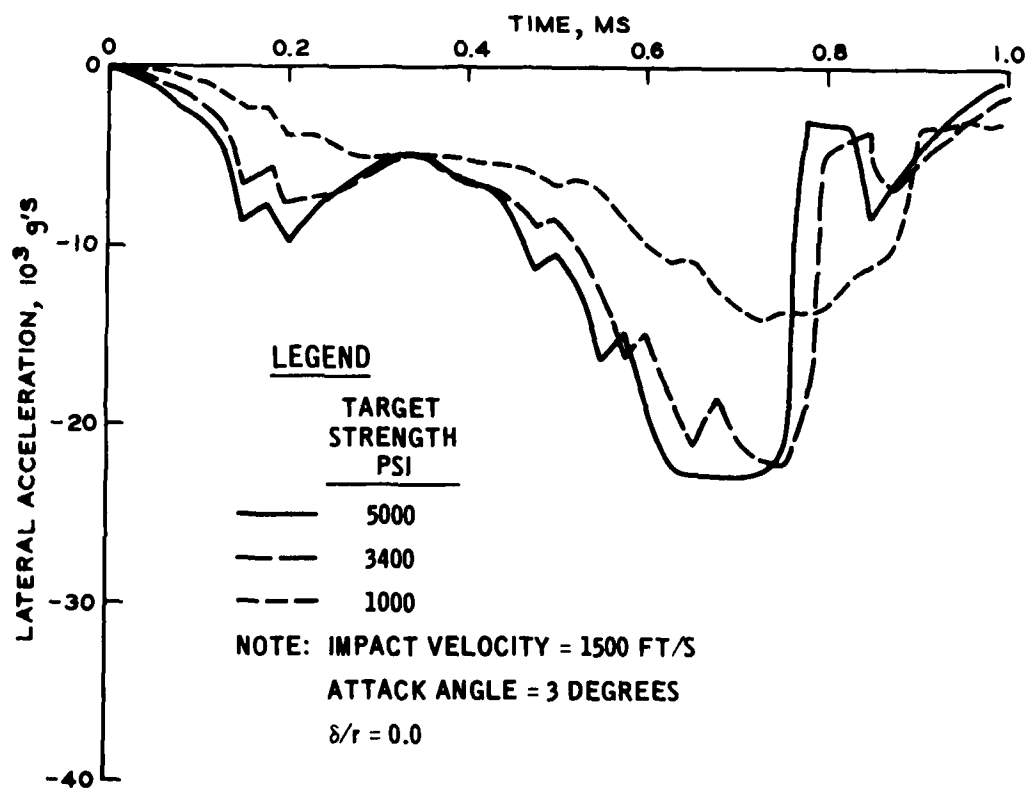
Figure 3.12 Calculated CG lateral acceleration for
             different values of target strength,
             Sandia RBT.
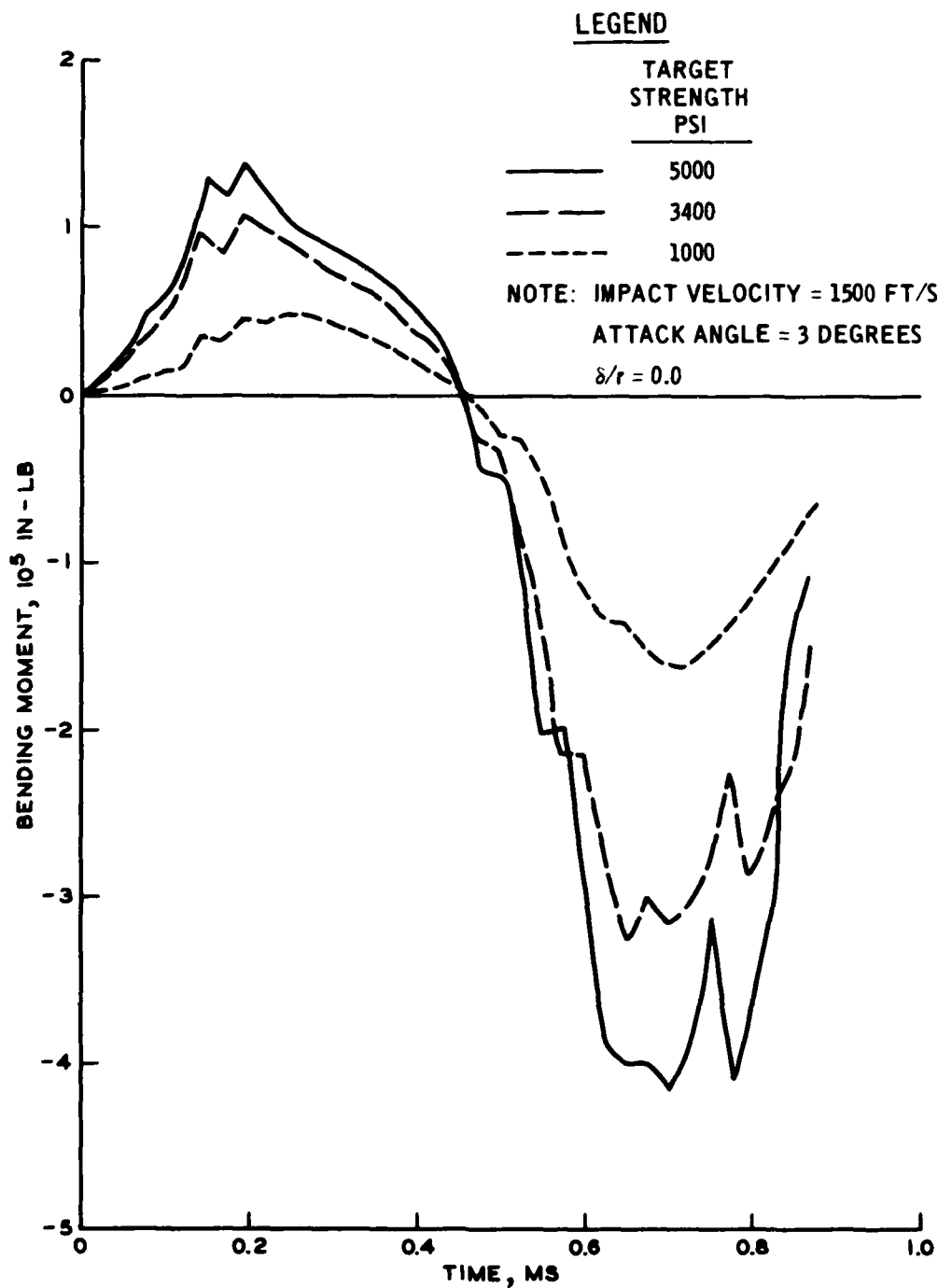
Figure 3.13 Calculated bending moment for different values of
target strength, Sandia RBT, section S.

41
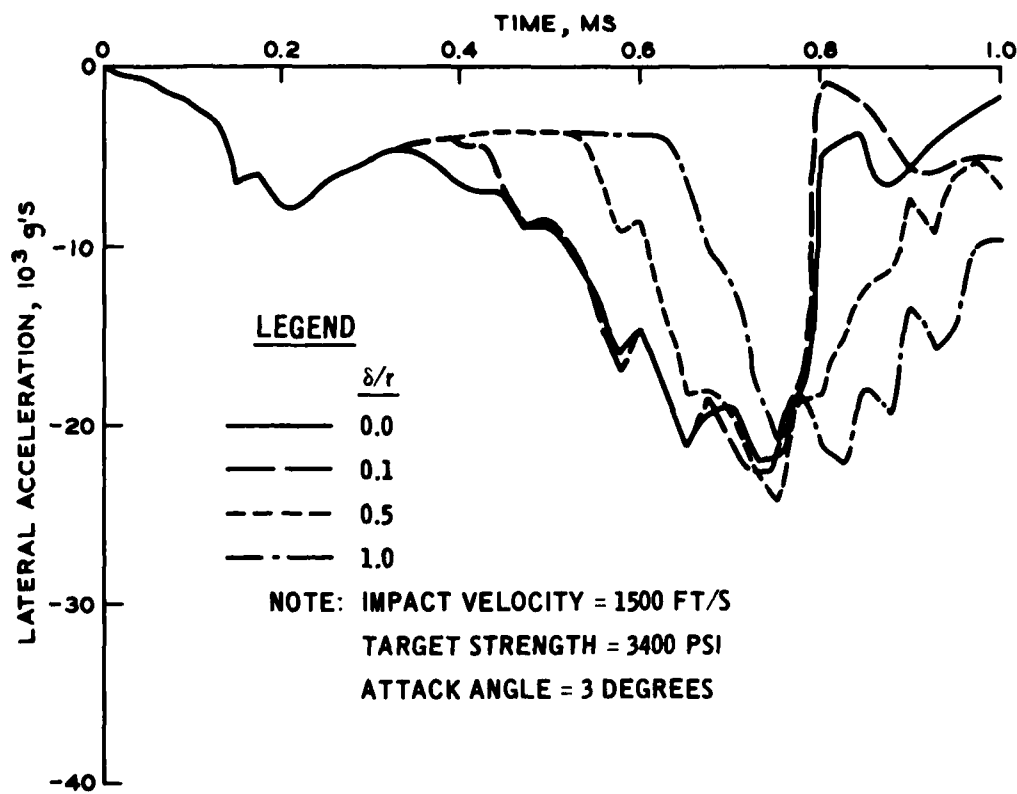
Figure 3.14 Calculated CG lateral acceleration for
different amounts of wake separation,
Sandia RBT.
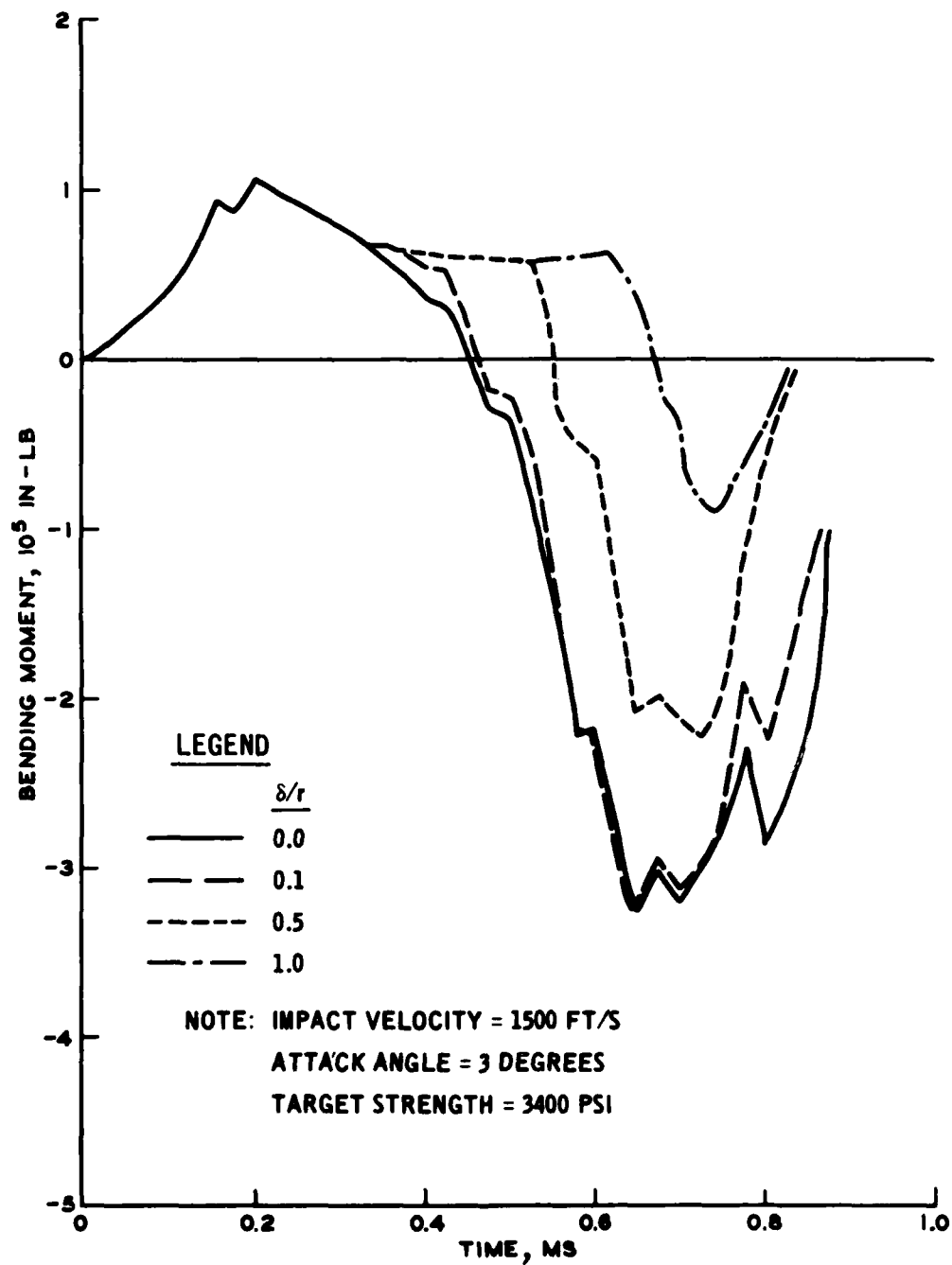
Figure 3.15 Calculated bending moment for different amounts of wake separation, Sandia RBT, section S.

PROJECTILE

0.47-SCALE EARTH PENETRATOR

WEIGHT = 38.2 LB

MAXIMUM DIAMETER = 3 IN

MOMENT OF INERTIA = 2160 LB-IN^2 (ABOUT CG)

NOSE SHAPE: 9.25 CRH OGIVE (BEVELED TIP)

$E_p = 2.8 \times 10^7$ PSI

$I_s = 3.98$ IN^4

$A_s = 7.07$ IN^2

$r_s = 1.5$ IN

```
0        5
|_____|
SCALE, INCHES
```

LATERAL DIRECTION

S

1050 FT/S
IMPACT VELOCITY

5°
ANGLE
OF
ATTACK

AXIAL
DIRECTION

TARGET

CONCRETE

DENSITY = 136 LB/FT^3

UNCONFINED STRENGTH = 6650 PSI

$\dfrac{\text{SHEAR MODULUS}}{\text{SHEAR STRENGTH}} \approx 400$

$\phi_1 = \phi_2 = 0$

$c_1 = c_2 = 3325$ PSI
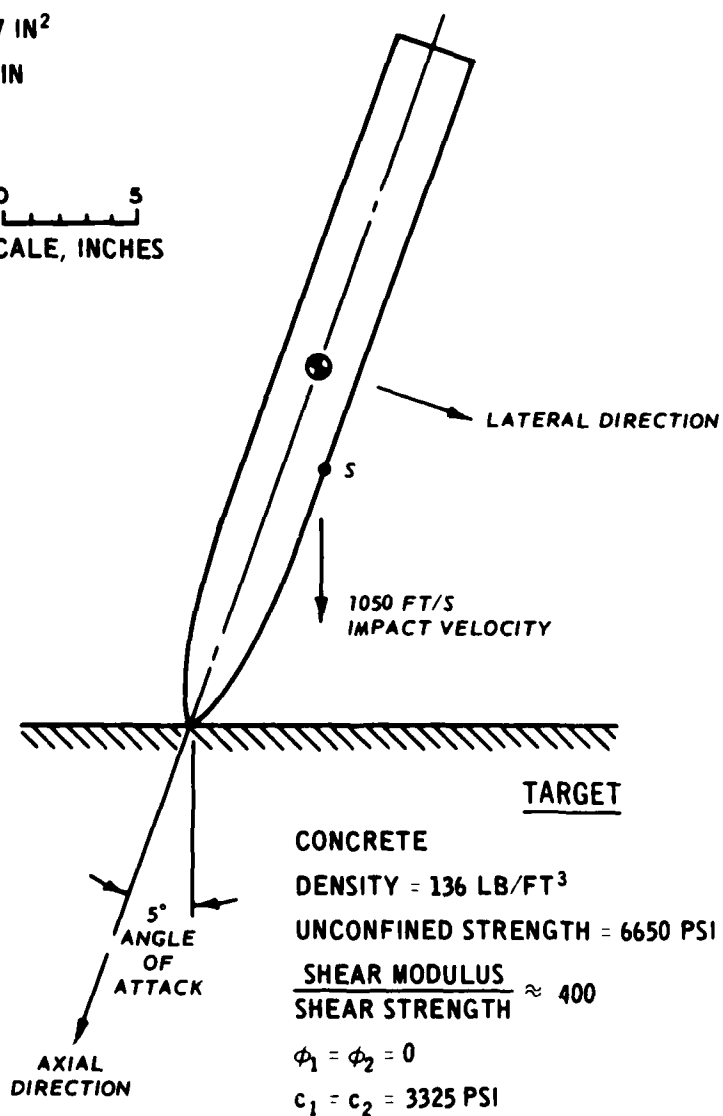
Figure 3.16 Projectile parameters, target properties, and impact
conditions for AVCO 1050-ft/s RBT.

PROJECTILE

0.47-SCALE EARTH PENETRATOR

WEIGHT = 36.6 LB

MAXIMUM DIAMETER = 3 IN

MOMENT OF INERTIA = 1937 LB-IN^2 (ABOUT CG)

NOSE SHAPE: 9.25 CRH OGIVE (BEVELED TIP)

$E_p = 2.8 \times 10^7$ PSI

$I_s = 3.98$ IN^4

$A_s = 7.07$ IN^2

$r_s = 1.5$ IN

$\alpha = 2, 5, 10$ DEGREES

0 _____ 5
SCALE, INCHES

LATERAL DIRECTION

S

1500 FT/S
IMPACT VELOCITY

α
ANGLE
OF
ATTACK

AXIAL
DIRECTION

TARGET

CONCRETE

DENSITY = 142 LB/FT^3

UNCONFINED STRENGTH = 3870 PSI

$\dfrac{\text{SHEAR MODULUS}}{\text{SHEAR STRENGTH}} \approx 400$

$\phi_1 = \phi_2 = 0$

$c_1 = c_2 = 1935$ PSI
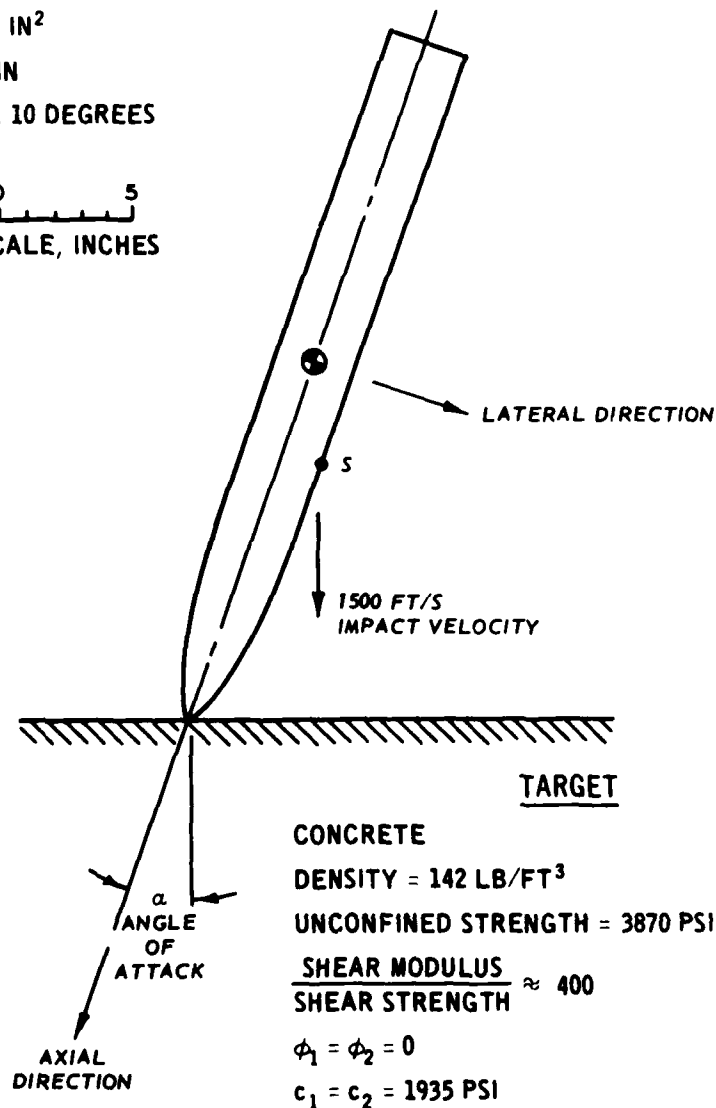
Figure 3.17 Projectile parameters, target properties, and impact
conditions for AVCO 1500-ft/s RBT.

STATION	LOCATION INCHES	SIGNIFICANCE
B	+5.78	NOSE BASE
CG	0.00	CENTER OF GRAVITY
F	+2.48	FORWARD ACCELEROMETER
R	-12.52	REAR ACCELEROMETER
S	+3.70	STRAIN GAGE
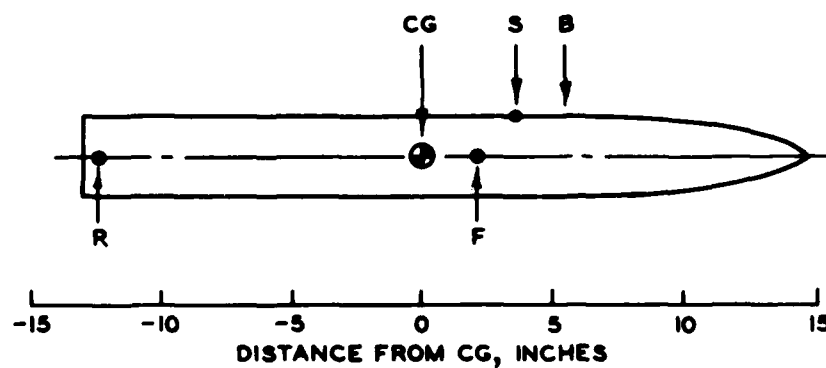
Figure 3.18 Axial location of strain gage and accelerometers
for projectile used in AVCO 1050-ft/s RBT.

STATION	LOCATION INCHES	SIGNIFICANCE
B	5.36	NOSE BASE
CG	0.00	CENTER OF GRAVITY
S	3.28	STRAIN GAGE
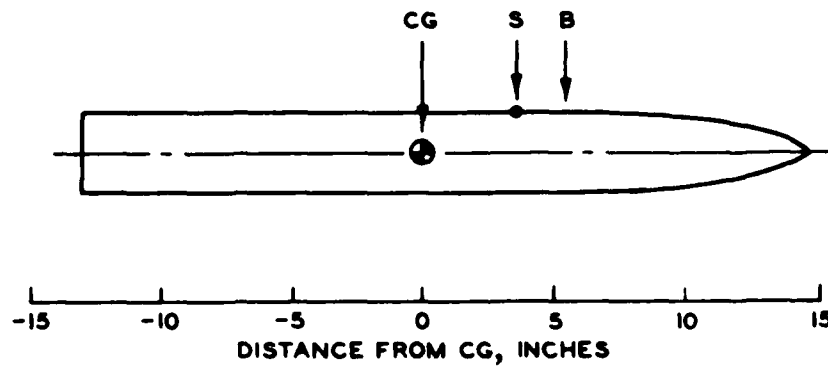
Figure 3.19 Axial location of strain gage for projectile used
in AVCO 1500-ft/s RBT.
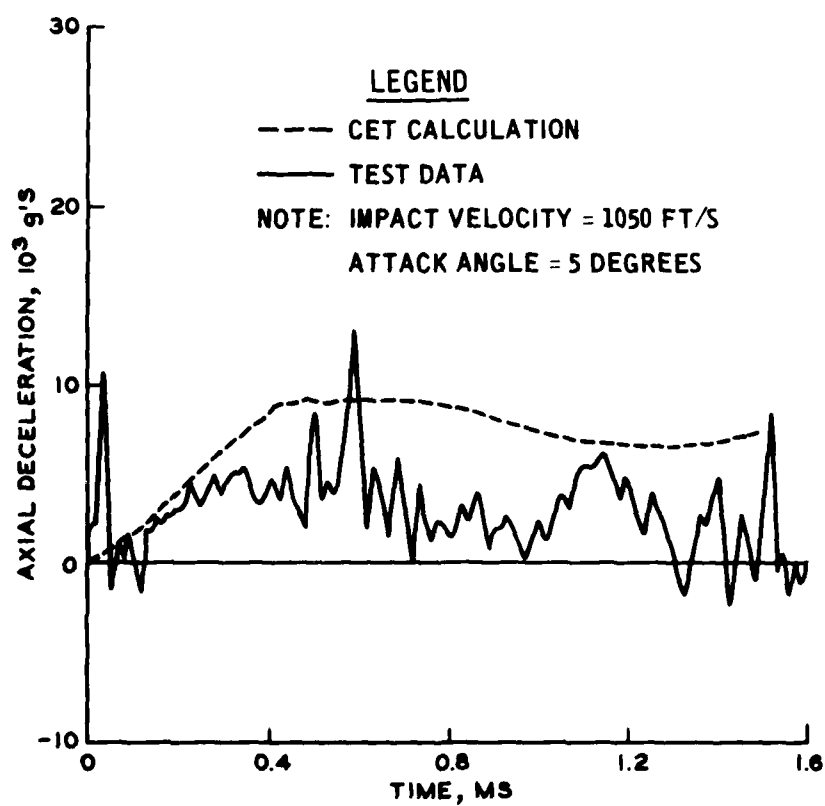
Figure 3.20 Comparison of calculated and measured axial decelerations for AVCO 1050-ft/s RBT, rear accelerometer.

48
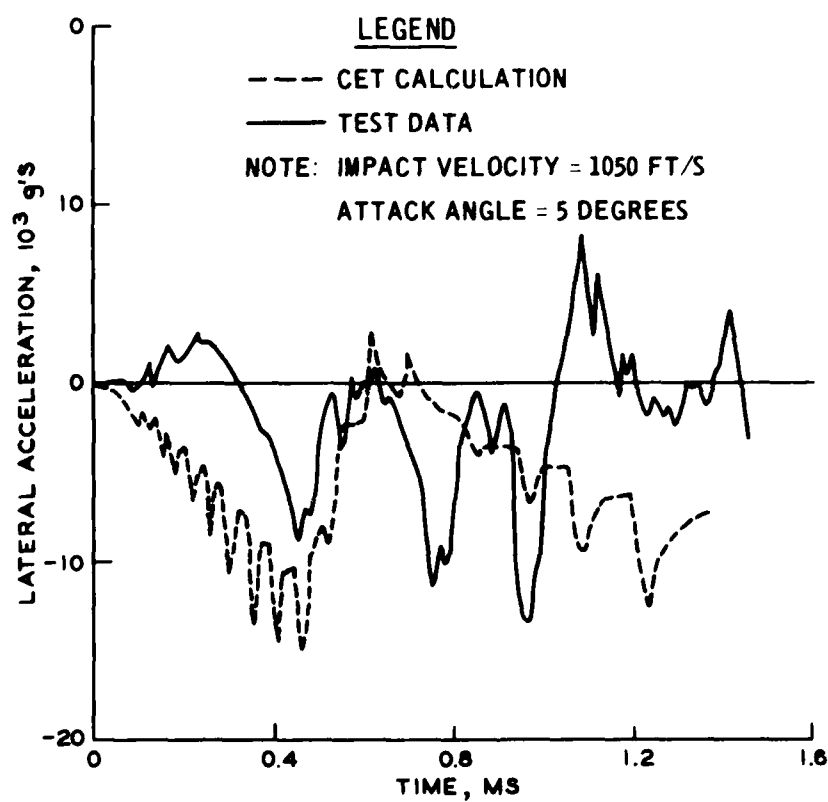
Figure 3.21   Comparison of calculated and measured lateral
accelerations for AVCO 1050-ft/s RBT, forward
accelerometer.
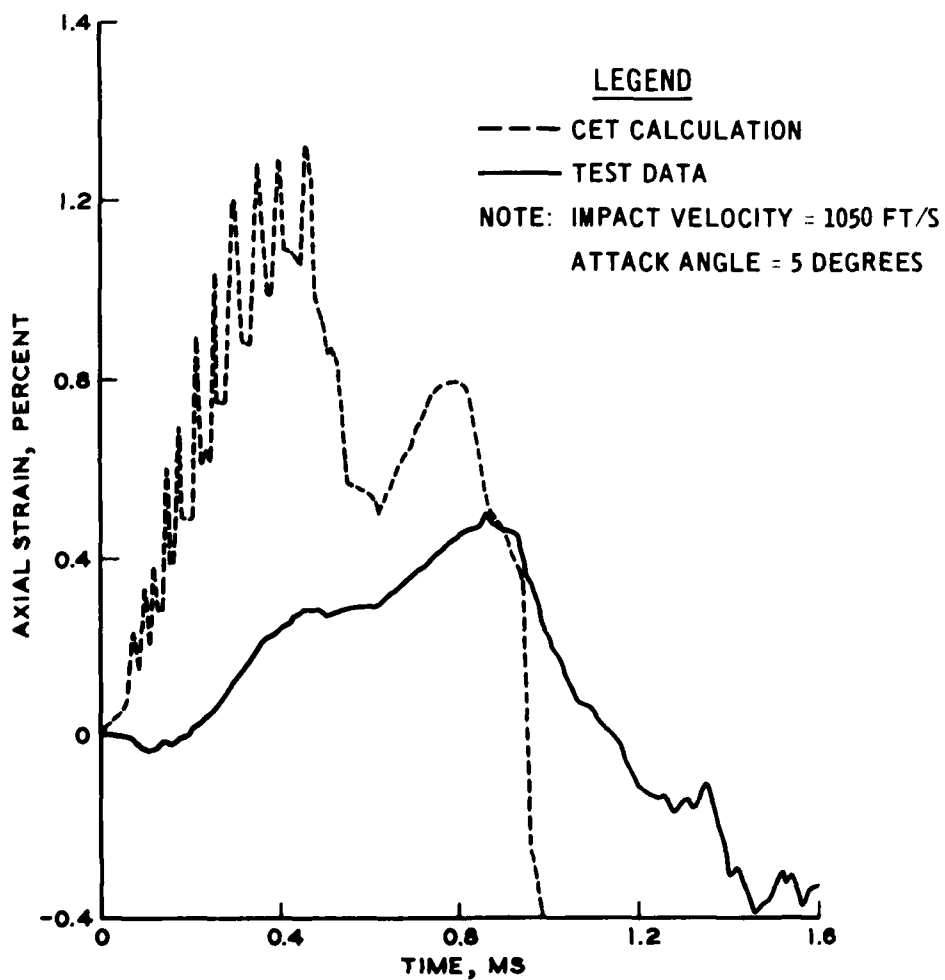
Figure 3.22   Comparison of calculated and measured strains
for AVCO 1050-ft/s RBT, strain gage S.

50
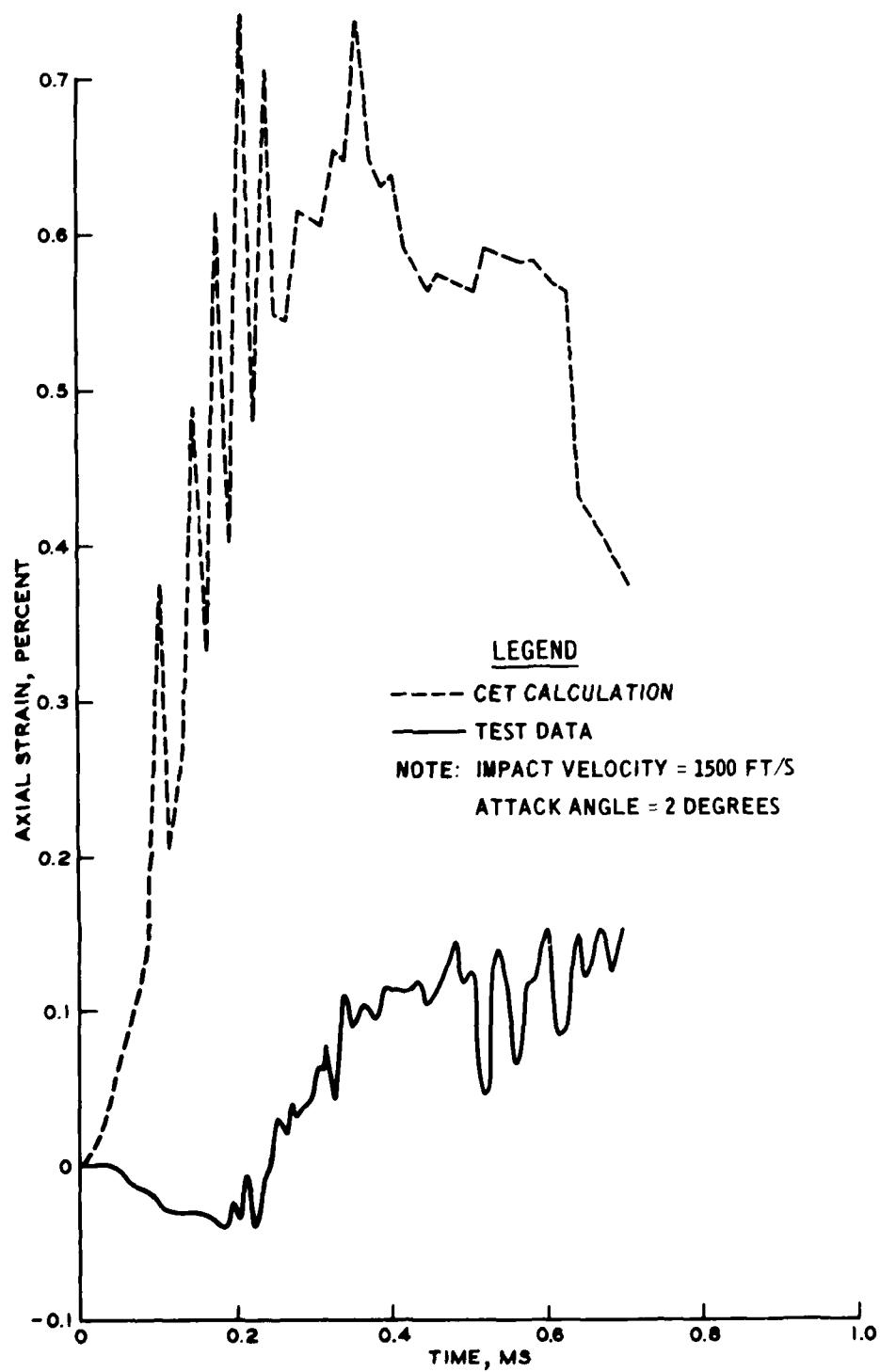
Figure 3.23   Comparison of calculated and measured strains for AVCO 2-degree RBT, strain gage S.
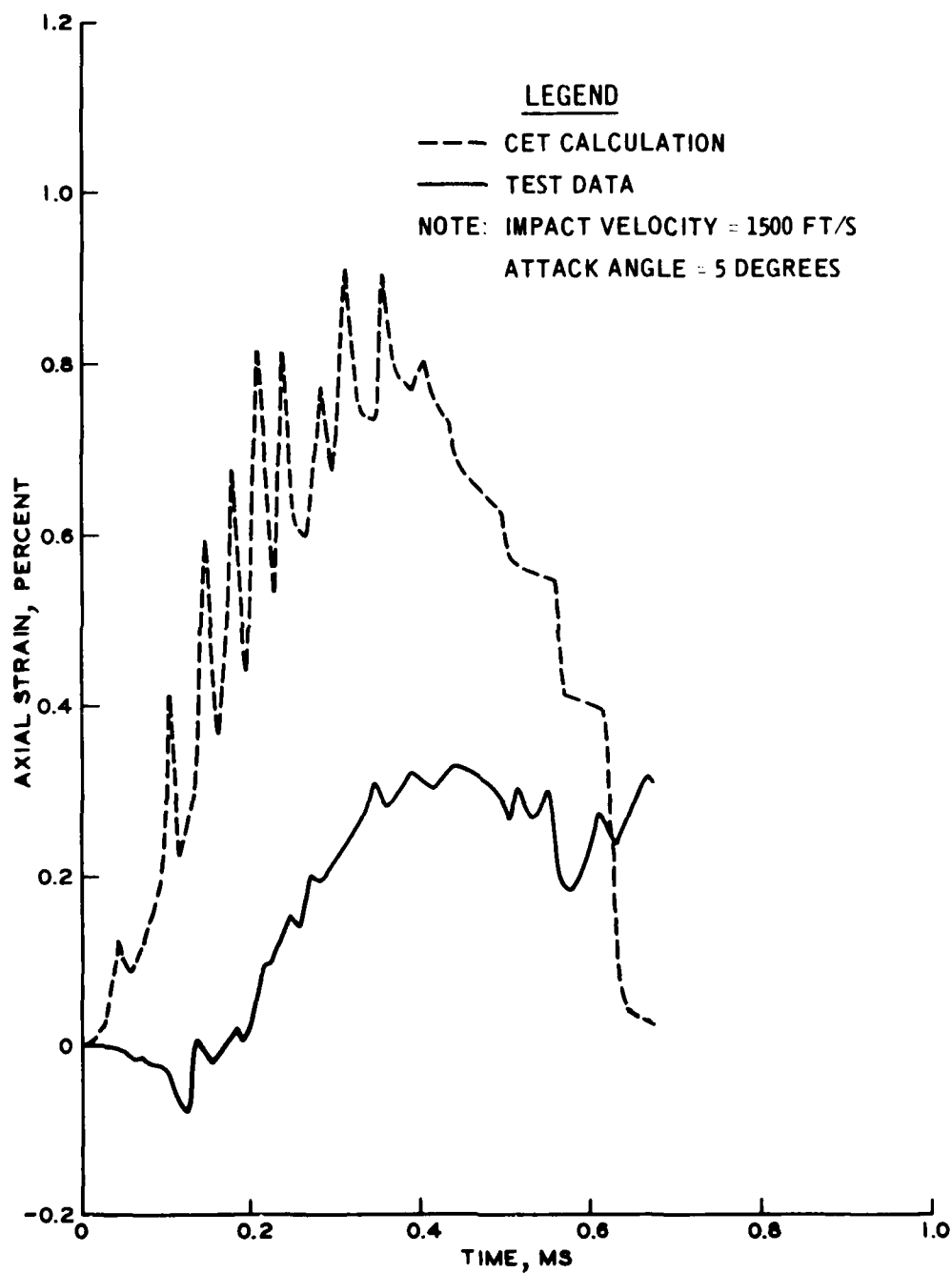
Figure 3.24 Comparison of calculated and measured strains
for AVCO 5-degree RBT, strain gage S.
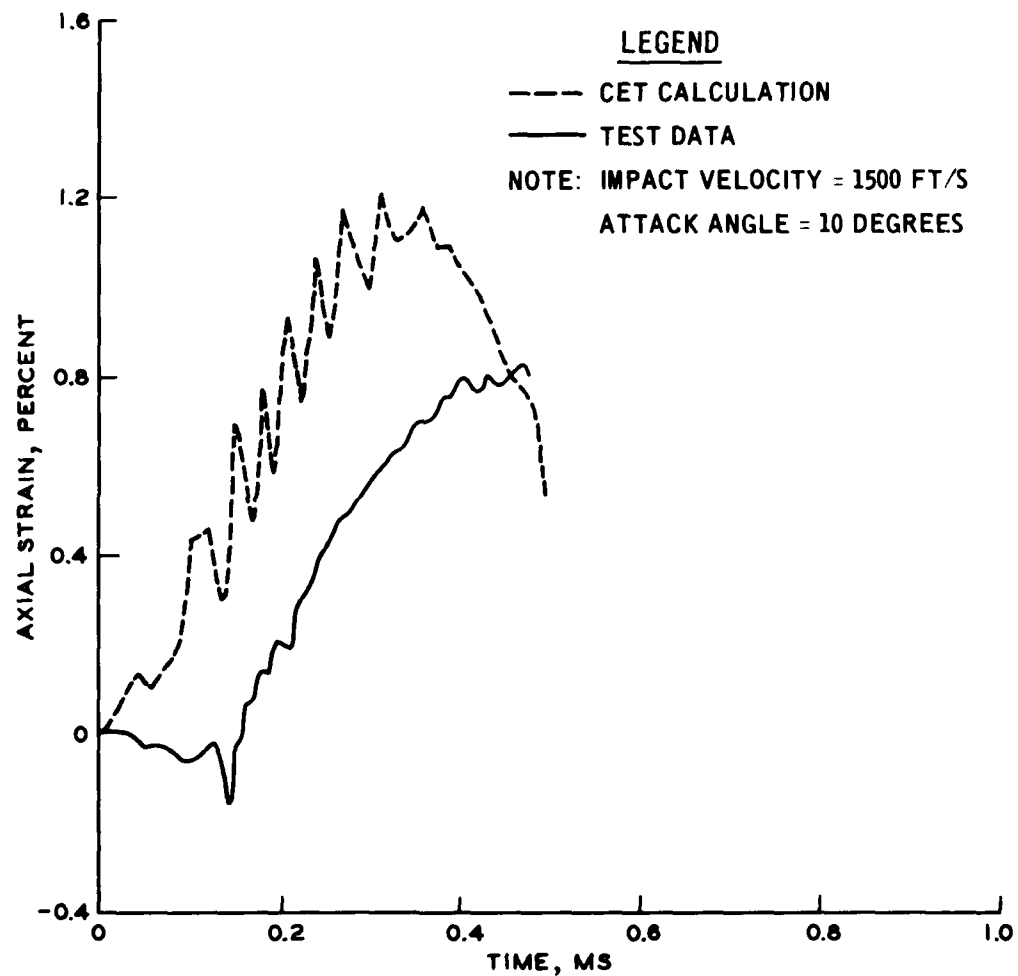
Figure 3.25 Comparison of calculated and measured strains
for AVCO 10-degree RBT, strain gage S.
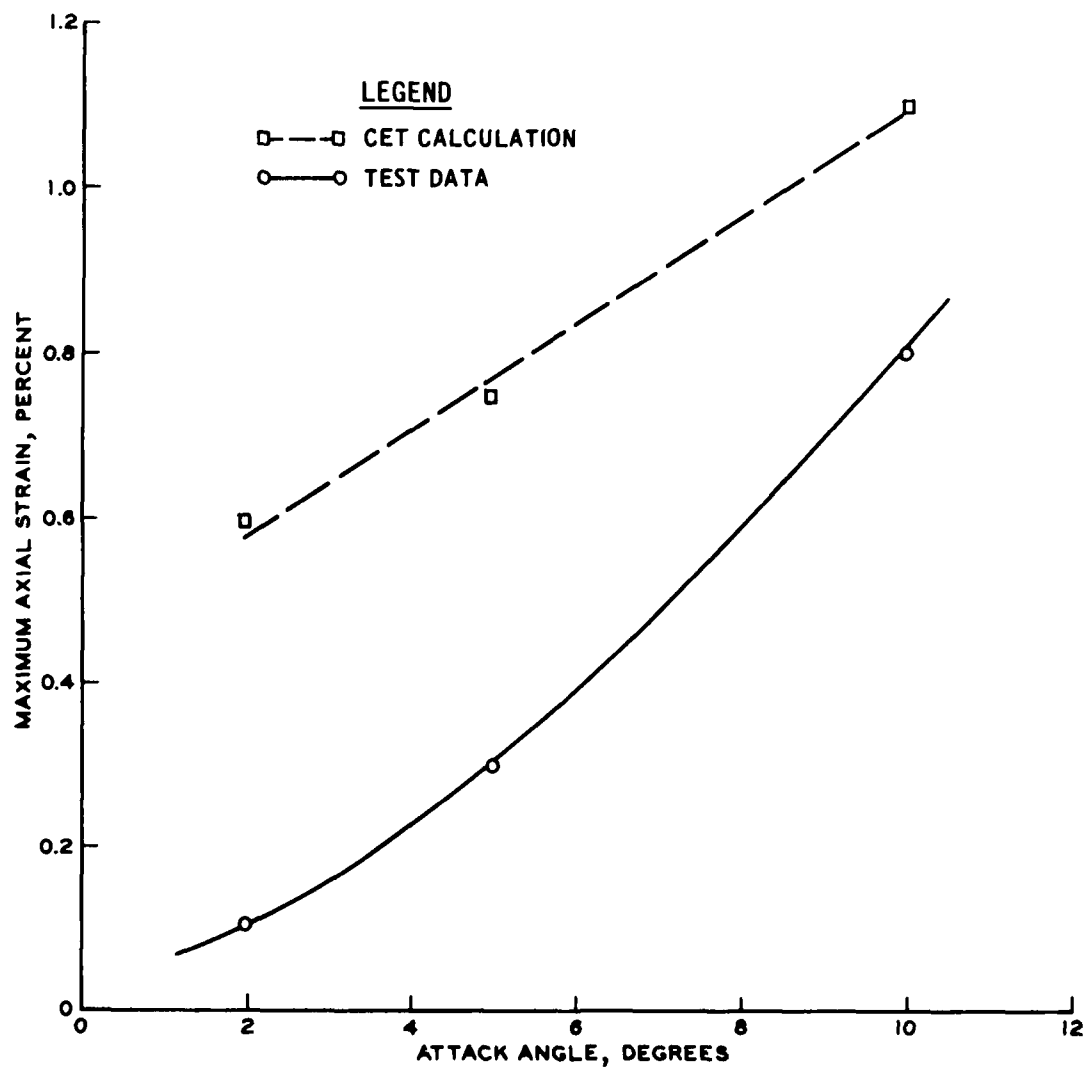
Figure 3.26   Comparison of calculated and measured strain
levels for AVCO 1500-ft/s RBT, strain gage S.

CHAPTER 4

CONCLUSIONS AND RECOMMENDATIONS

The CET analysis for normal impact and penetration has been extended to include non-normal impact for small angles of attack (less than 10 degrees) and hard targets (such as rock and concrete). The extension was accomplished without introducing any new target parameters (empirical or otherwise), the primary assumption being that the lateral and axial force distributions can be specified separately.

The non-normal CET analysis was installed in a modified version of the AVCO DAFL code, replacing AVCO's definition of the force distribution on the projectile. The modified code was then used to make calculations for comparison with non-normal RBT data obtained by Sandia Laboratories and by AVCO Corporation.

The calculated results reproduced the Sandia data fairly well, except for a time delay.[1] The calculations, however, overpredicted the AVCO strain and acceleration data by a factor of 2 to 6, depending on the angle of attack. The AVCO targets were apparently too small to simulate the resistance of a half-space for depths greater than 40 percent of the nose length or times greater than 0.2 ms. In the AVCO tests, the ratio of target diameter to projectile diameter was 5; in the Sandia tests, this ratio was 30.

The agreement between the calculations and the Sandia data is encouraging, but more tests are needed to check the theory at angles of attack other than 3 degrees. If the trends observed in the AVCO tests are borne out in future tests with larger targets, then the CET analysis may require some modification. Nevertheless, the theory as it stands seems to be accurate enough for projectile design calculations in the meantime.

---

[1] The time delay is apparently caused by nonrigid projectile response to the rapidly varying applied loads. Appendix B presents the results of a dynamic structural analysis, revealing a similar internal-response time delay.

REFERENCES

1. F. R. Lascher, et al.; "Determination of Penetration Forcing Function Data for Impact Fuzes" (Interim Final Report, Phase I); Report No. AVSD-0074-75-RR, 15 June 1974; AVCO Corporation, Wilmington, Mass.

2. R. S. Bernard and D. C. Creighton; "Projectile Penetration in Earth Materials: Theory and Computer Analysis;" Technical Report S-76-13, February 1976; U. S. Army Engineer Waterways Experiment Station, CE, Vicksburg, Miss.

3. W. R. Kampfe; "DNA 1/3 Scale Pershing Penetrator Tests;" Letter report to Defense Nuclear Agency, dated October 1977; Sandia Laboratories, Albuquerque, N. Mex.

4. D. C. Creighton; "Correlation of Reverse Ballistic Test Data;" Letter report to Defense Nuclear Agency, dated December 1977; U. S. Army Engineer Waterways Experiment Station, CE, Vicksburg, Miss.

5. "Impact and Penetration Technology: Progress Report No. 2;" Prepared for Defense Nuclear Agency, June 1975; AVCO Corporation, Wilmington, Mass.

6. "Impact and Penetration Technology: Progress Report No. 3;" Prepared for Defense Nuclear Agency, August 1975, AVCO Corporation, Wilmington, Mass.

7. D. Henderson, "Impact and Penetration Technology Program Parameter Study," Report No. DNA3921F, May 1976, AVCO Systems Division, Wilmington, Mass.

APPENDIX A

CAVITY EXPANSION THEORY

Reference 2 documents an analysis of quasi-static spherical cavity expansion in an elastic-plastic material.[1] This analysis, known as the Cavity Expansion Theory (CET), is the basis of the normal-impact penetration theory (Reference 2). For non-normal impact and penetration in <u>hard</u> targets, the effects of overburden and compressibility are negligible, and the basic assumptions and results of the CET are those given below.

Consider an infinite medium surrounding a spherical cavity that slowly expands from zero initial radius to instantaneous radius $a > 0$. Denoting the radial and circumferential stresses[2] by σ_r and σ_θ, respectively, the equations that describe the bilinear failure envelope HBA (Figure A.1) on segments HB and BA are

$$\text{Segment HB:} \quad \sigma_r - \sigma_\theta = (\sigma_r + \sigma_\theta) \sin \phi_1 + 2c_1 \cos \phi_1 \qquad \text{(A.1)}$$

$$\text{Segment BA:} \quad \sigma_r - \sigma_\theta = (\sigma_r + \sigma_\theta) \sin \phi_2 + 2c_2 \cos \phi_2 \qquad \text{(A.2)}$$

The quantities c_1 and ϕ_1 are, respectively, the values of the cohesion and the internal friction angle for segment HB; c_2 and ϕ_2 are the corresponding values for segment BA.

The material surrounding the cavity is divided into separate elastic and plastic regions, as shown in Figure A.2. Denoting the radial position by the symbol r, the relation between σ_r and σ_θ in the region $b \leq r \leq h$ is given by Equation A.1, and the corresponding relation in the region $a \leq r \leq b$ is given by Equation A.2. The geometry is spherically symmetric, and the material equation of equilibrium is

---

[1] Reference numbers refer to similarly numbered items in the References at the end of the main text.
[2] Compressive stresses and strains are considered positive.

57

$$\frac{d\sigma_r}{dr} + \frac{2}{r} (\sigma_r - \sigma_\theta) = 0 \qquad (A.3)$$

Upon integrating Equation A.3 from $r = a$ to $r = \infty$, it is found that the radial stress σ_s at the cavity wall is

$$\sigma_s = (c_2 \cot \phi_2 - c_1 \cot \phi_1) \left(I_{12}^{\beta/3} - 1 \right)$$

$$+ \frac{c_2 \cos \phi_2 (1 + \sin \phi_1) - c_1 \cos \phi_1 (1 + \sin \phi_2)}{\sin \phi_1 - \sin \phi_2} \qquad (A.4)$$

where

$$I_{12} = \frac{I_1}{I_2^{3/\gamma}} \qquad (A.5)$$

$$\gamma = \frac{4 \sin \phi_1}{1 + \sin \phi_1} \qquad (A.6)$$

$$\beta = \frac{4 \sin \phi_2}{1 + \sin \phi_2} \qquad (A.7)$$

$$I_1 = \left(\frac{3}{2} \varepsilon_* \right)^{-1} \qquad (A.8)$$

$$I_2 = \frac{(3 - \sin \phi_1) \left[c_2 \cos \phi_2 - c_1 (1 + \cot \phi_1) \sin \phi_2 \right]}{3(\sin \phi_1 - \sin \phi_2) c_1 \cot \phi_1} \qquad (A.9)$$

The quantity I_1 is the material rigidity index, and ε_* is the radial strain at the onset of plastic behavior (which is the same as the axial strain to failure in a triaxial compression test).

The von Mises condition ($c_1 = c_2 \equiv c$, $\phi_1 = \phi_2 = 0$) is the simplest failure condition for which Equation A.4 is applicable. In this case,

the expression for σ_s reduces to

$$\sigma_s = \frac{4}{3} c(1 + \ell n \, I_1) \qquad (A.10)$$

If the material is governed by the linear Mohr-Coulomb condition ($c_1 = c_2 \equiv c$, $\phi_1 = \phi_2 \equiv \phi > 0$), then Equation A.4 becomes

$$\sigma_s = \frac{3(1 + \sin \phi)(I_1^{\gamma/3} - 1)}{3 - \sin \phi} \, c \cot \phi \qquad (A.11)$$

The failure criterion for some materials may be approximated using a bilinear condition in which $\phi_1 > 0$ and $\phi_2 = 0$ (von Mises limit). When this situation arises, the expression for σ_s simplifies to

$$\sigma_s = \frac{c_2(1 + \sin \phi_1) - c_1 \cos \phi_1}{\sin \phi_1} + \frac{4}{3} c_2 \, \ell n \, I_{12} \qquad (A.12)$$

If $I_{12} \leq 1$ (when $0 < c_1 < c_2$, $0 < \phi_2 < \phi_1$), then the entire plastic region is governed by segment HB of the failure envelope. In this case, c is set equal to c_1, ϕ is set equal to ϕ_1, and σ_s is given by Equation A.11.
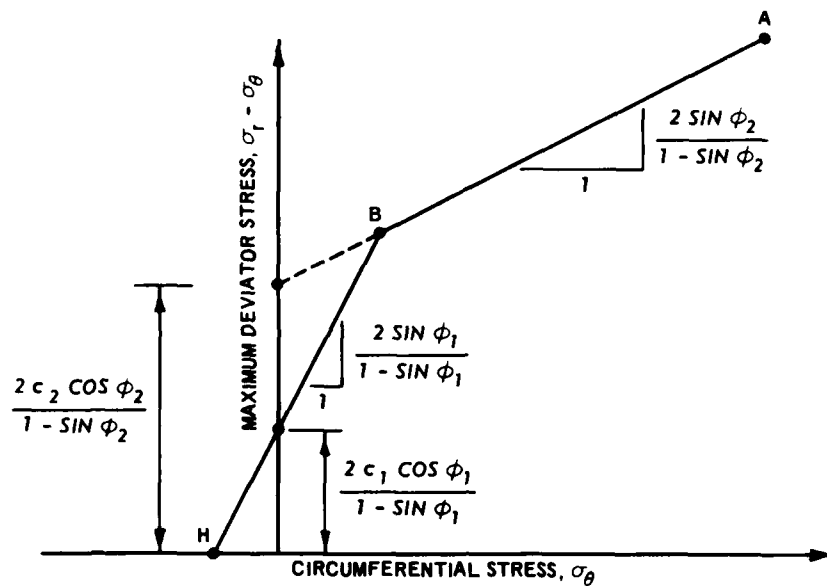
Figure A.1 Bilinear failure envelope.
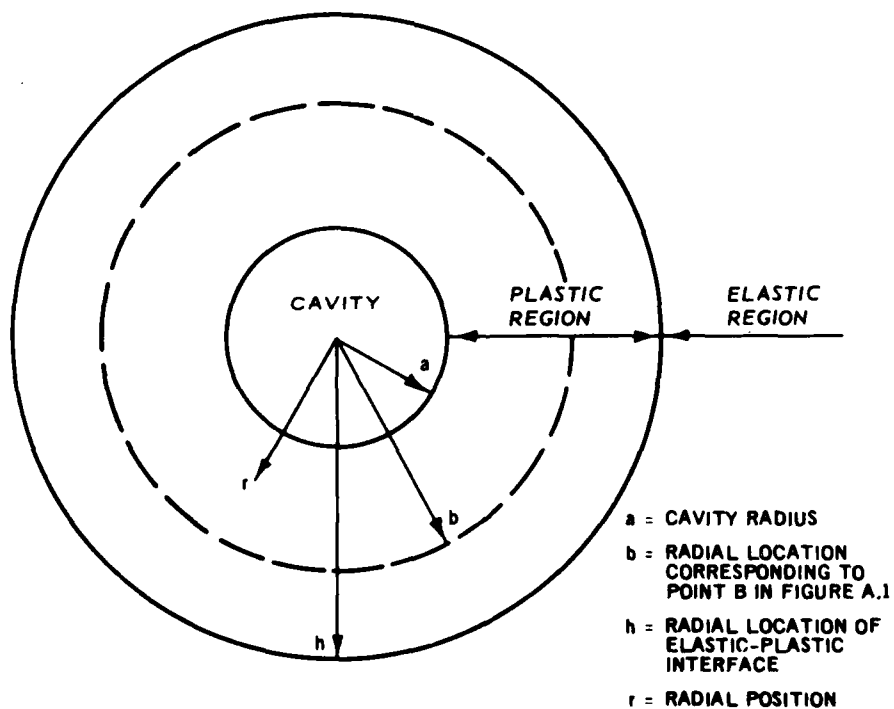
Figure A.2 Slowly expanding spherical cavity in an infinite elastic-plastic medium.

60

APPENDIX B

NONRIGID PROJECTILE RESPONSE

Chapter 3 discusses briefly projectile deformation under static load, ignoring the complications introduced by a rapidly changing (dynamic) load. Although dynamic structural-response analysis is beyond the scope of Chapters 2 and 3, it seems to explain in part the time delay in the RBT data.

T. Belytschko[1] has used the CET-calculated external loads in a lumped-parameter computer code, calculating dynamic projectile response for the 3-degree Sandia RBT's. Figures B.1 and B.2 show Belytschko's lateral-acceleration results compared with the original rigid-body calculations (Chapter 3). A time delay is clearly evident in the non-rigid response for the rear accelerometer.

A comparison of the nonrigid calculations with the test data (Figures B.3 through B.5) shows that the predicted initial response is indeed closer to the measured initial response than are the rigid-body calculations. The late-time accelerations, however, are still out of phase with the data. The best agreement occurs for the axial strain date (Figure B.5).

These nonrigid response calculations do not fully reconcile the CET predictions with the RBT data. Nevertheless, the appearance of a time delay (due solely to nonrigidity) in the calculations is evidence that the delays observed in Chapter 3 probably arise from the same source.

---

[1] Personal communication dated June 1978 from T. Belytschko, Inc., Chicago, Ill., to R. Bernard, Soil Dynamics Division, Soils and Pavements Laboratory.
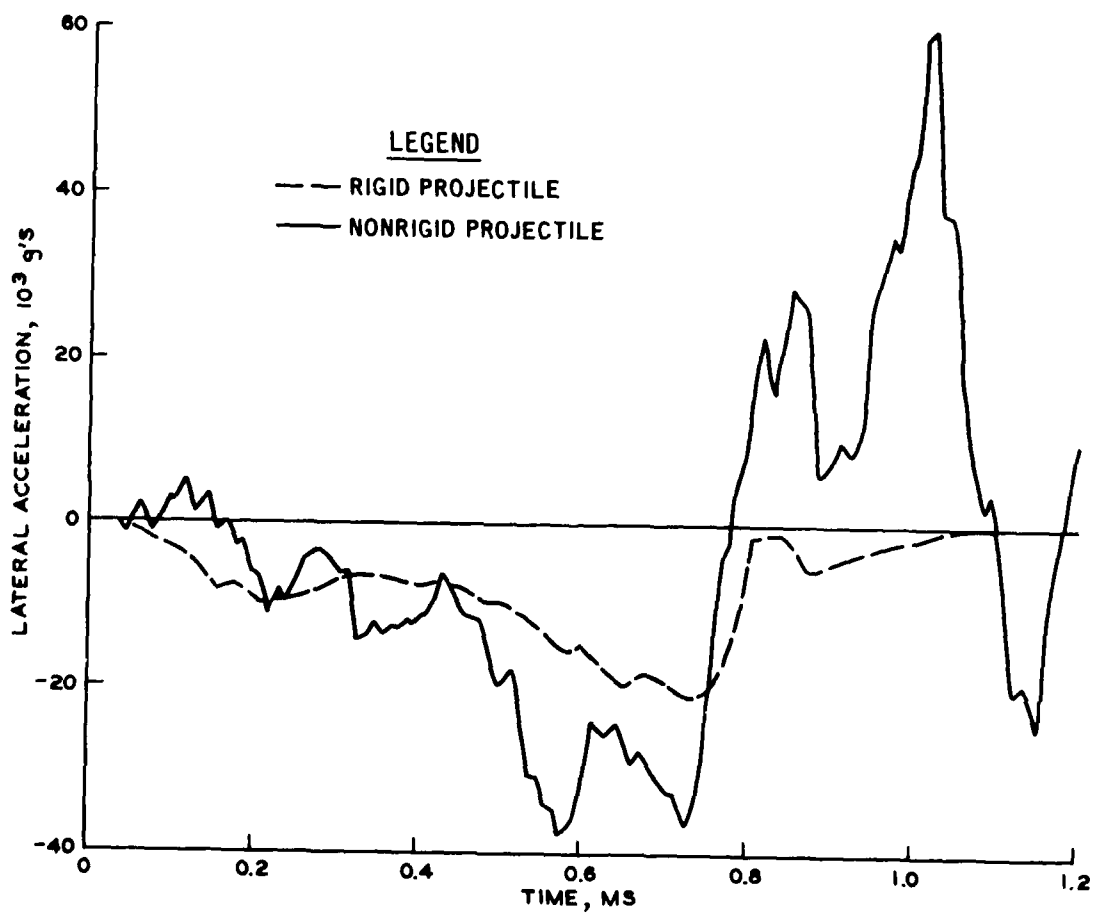
Figure B.1   Comparison of rigid and nonrigid projectile-response
calculations for forward accelerometers, Sandia RBT.
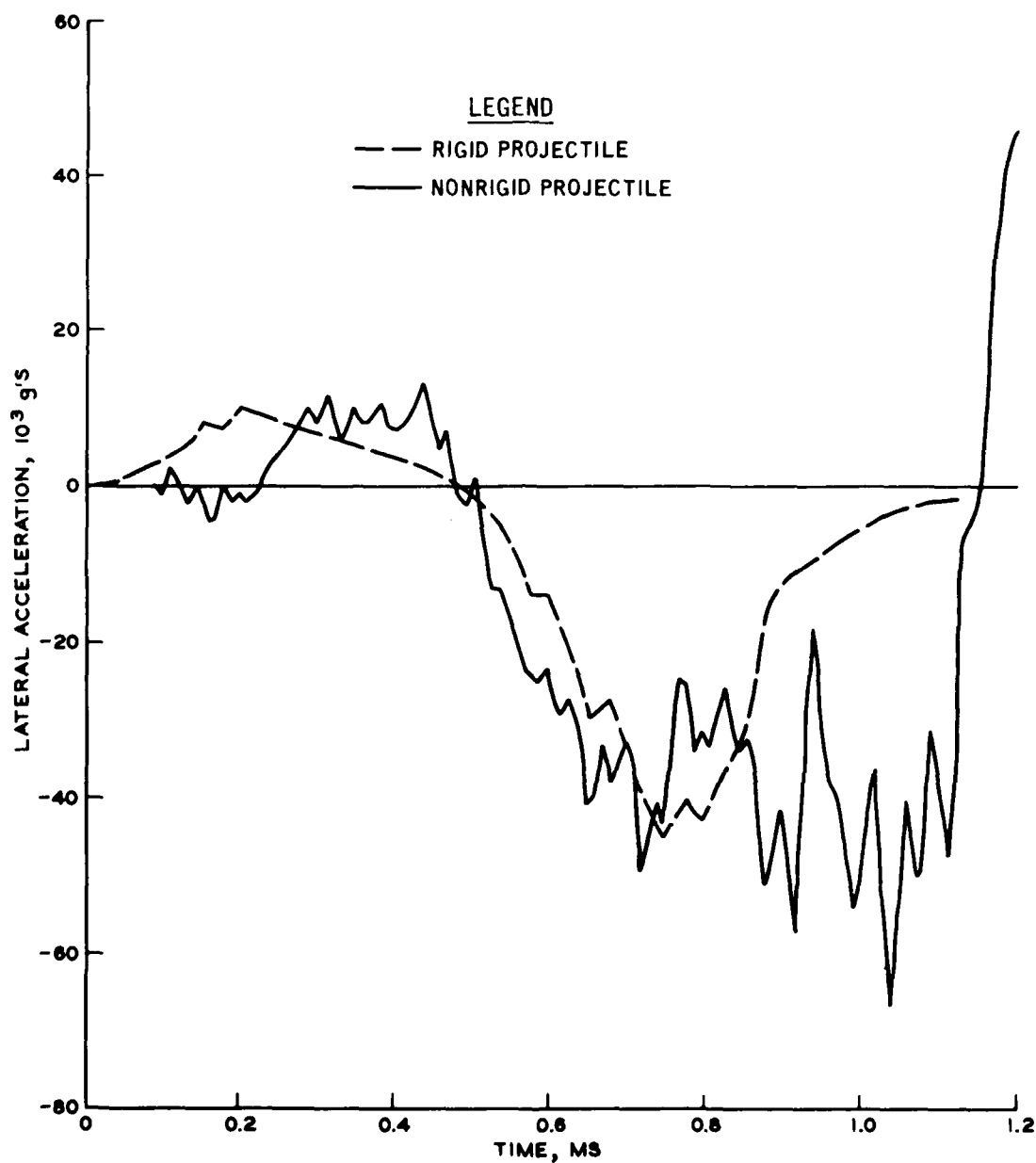
Figure B.2 Comparison of rigid and nonrigid projectile-response calculations for rear accelerometer, Sandia RBT.

63
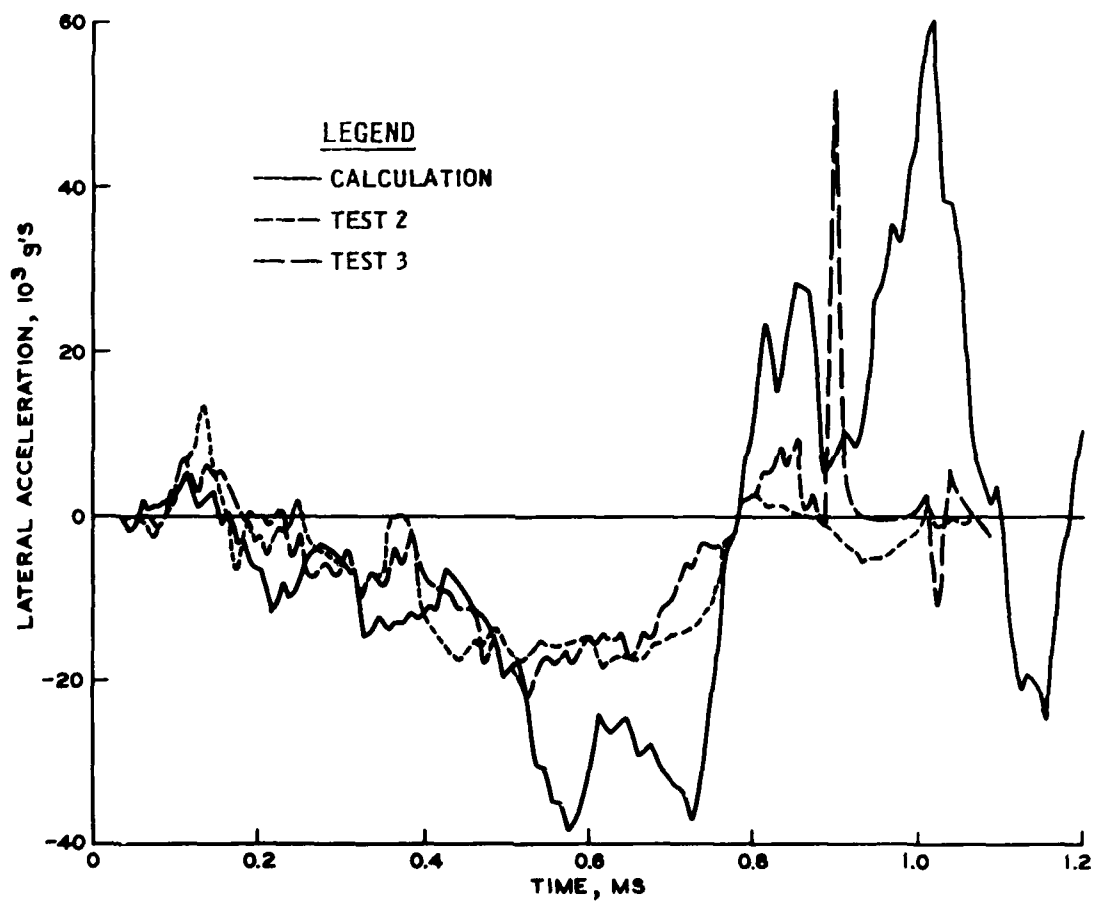
Figure B.3   Comparison of measured lateral accelerations
with dynamic structural-response calculation
for forward accelerometer, Sandia RBT.
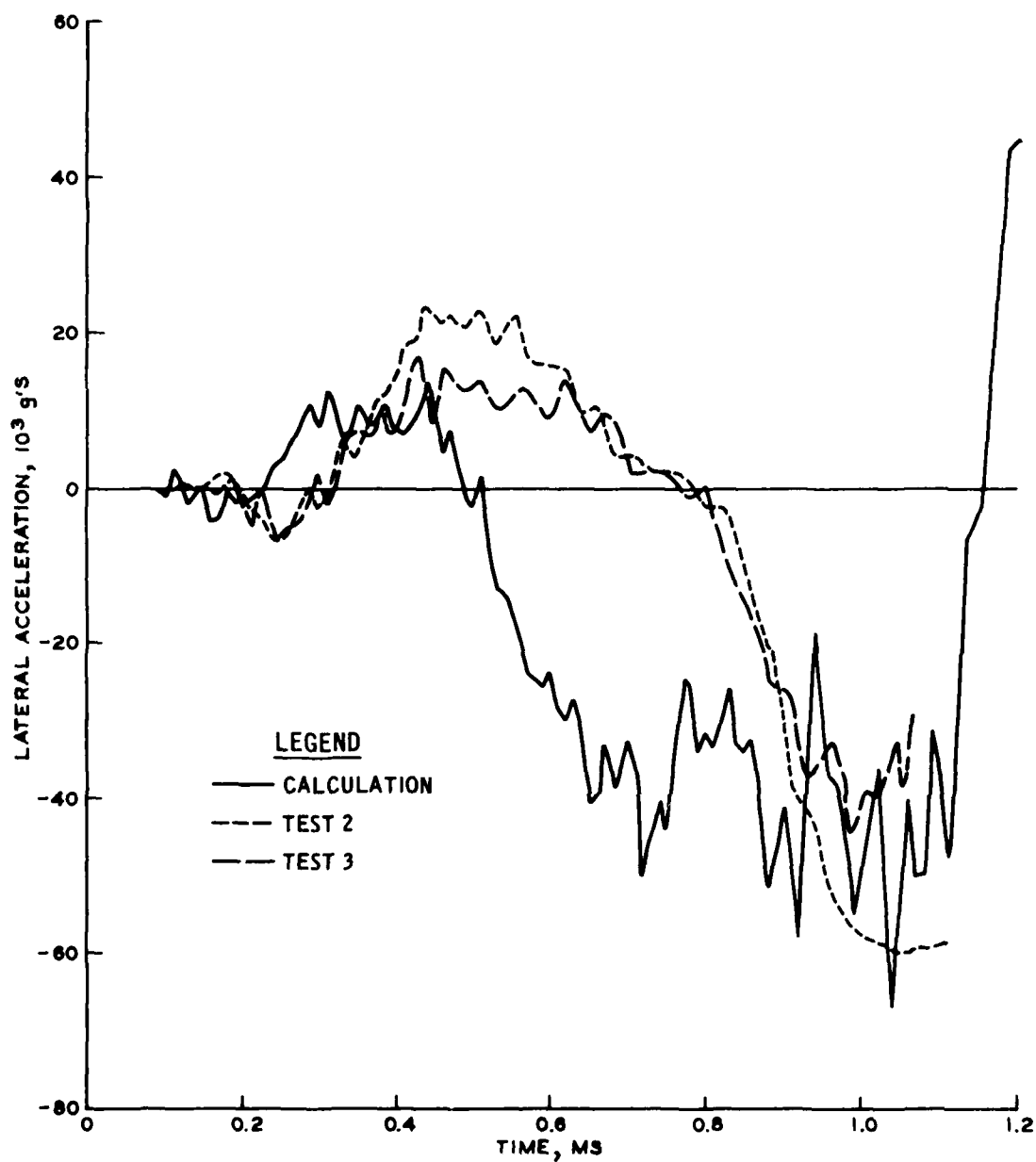
Figure B.4   Comparison of measured lateral accelerations
with dynamic structural-response calculation
for rear accelerometer, Sandia RBT.

65
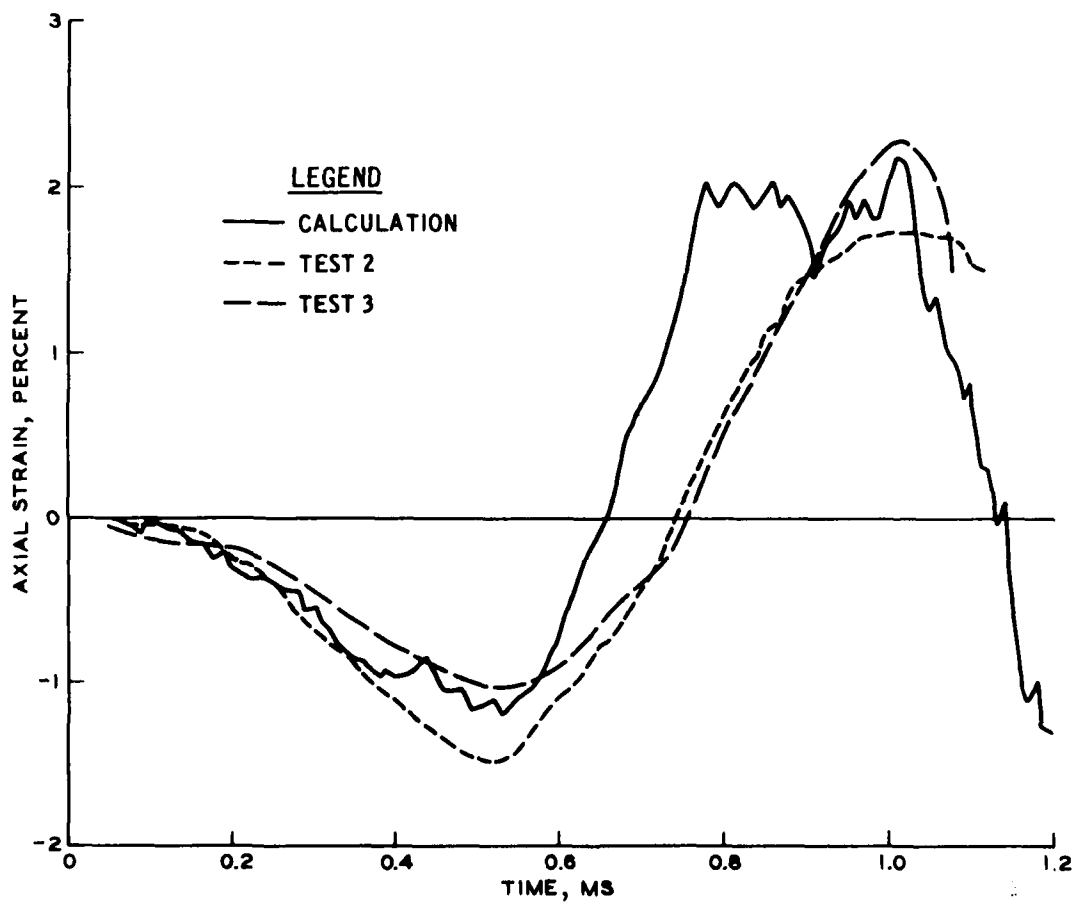
Figure B.5 Comparison of measured axial strains with dynamic
structural-response calculation for strain gage
S, Sandia RBT.

66

APPENDIX C

COMPARISON OF CET AND AVCO CALCULATIONS

At present, the AVCO DAFL seems to be the only viable alternative to the CET analysis for calculating non-normal projectile loads. Although the DAFL formulation is quite different from the CET analysis, it is worthwhile to compare the predictions of the two for the same projectile, target, and impact conditions.

D. Henderson of AVCO has conducted an extensive parameter study (Reference 7) with the DAFL. The baseline projectile and concrete target from this study have been chosen for comparison of DAFL and CET predictions. The projectile parameters are shown in Figure C.1. The nominal properties of the concrete are as follows: $Y = 5000$ psi, $\rho = 4.66$ slug/ft^3, and $E = 3 \times 10^6$ psi.

Figure C.2 compares the results for maximum lateral CG acceleration versus angle of attack. In these calculations, the CET analysis consistently overshoots the AVCO results by about 50 percent. The discrepancy, however, is in the absolute magnitude of the acceleration; the slope of the curves is about the same for the same impact velocity.

Since mechanical properties are usually more readily obtainable than are AVCO's empirical target parameters, the CET analysis is the easier method to use for before-the-fact calculations in untried targets. Nevertheless, when used by an experienced analyst such as Henderson, the DAFL has generally proved to be capable of accurate predictions. Both methods should be used whenever possible.
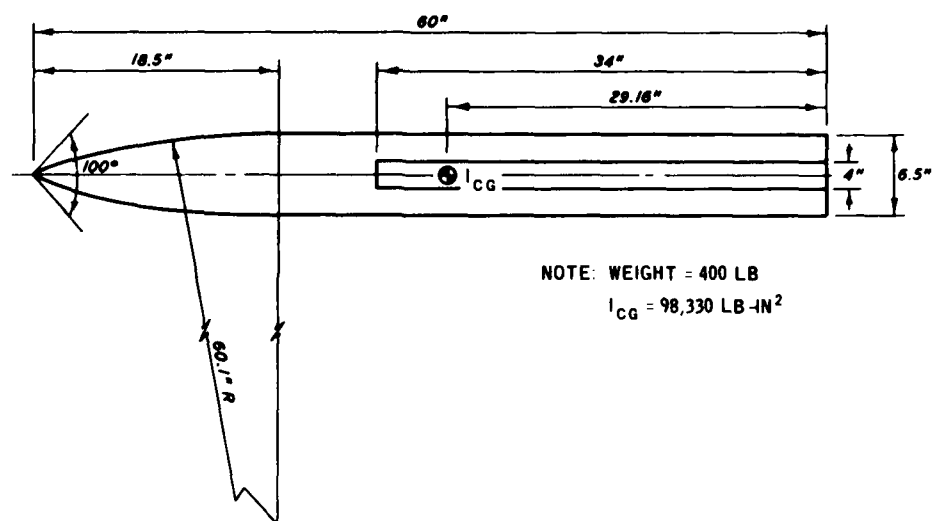
Figure C.1 Baseline AVCO projectile parameters.
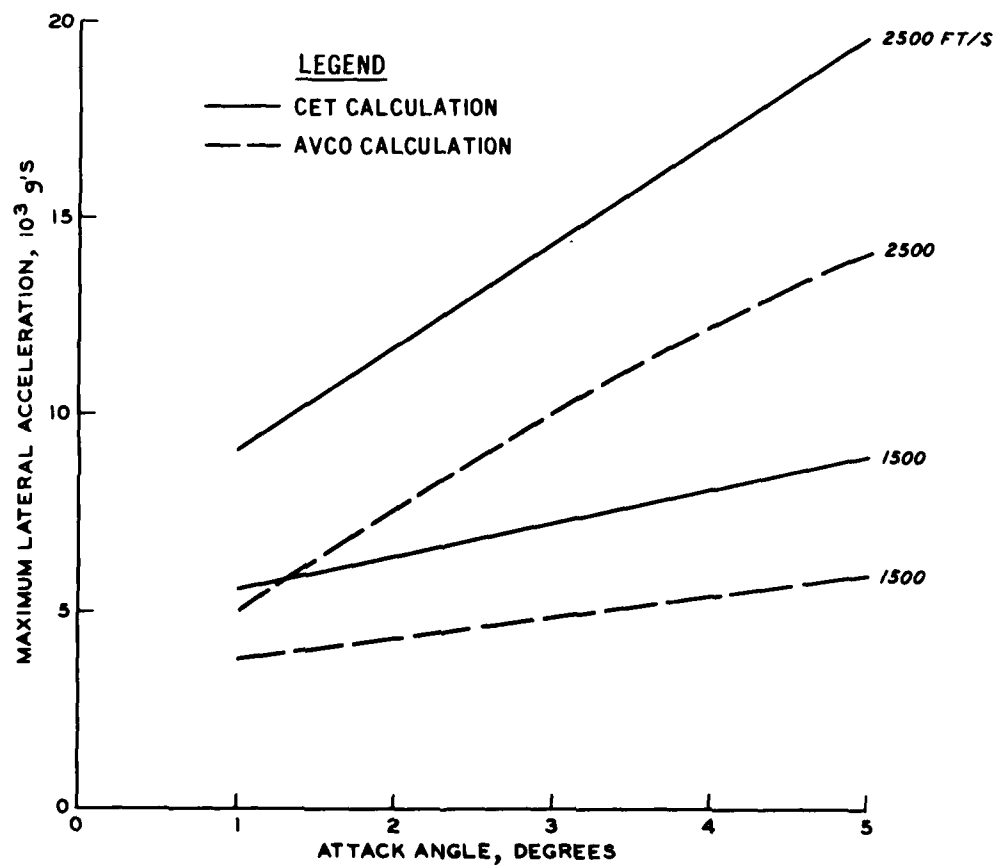
Figure C.2   Comparison of AVCO and CET calculations
of lateral acceleration.

APPENDIX D

NOTATION

a   Spherical cavity radius

A   Surface area

A_s Cross-sectional area of projectile at section C

b   Radial position corresponding to break point on bilinear failure envelope

c   Material cohesion

c_1, c_2 Value of cohesion describing bilinear failure envelope

CG   Center of gravity

dA   Differential surface area

$dM(z)$ Point distribution of mass along the projectile axis

E   Young's modulus for target

E_p Young's modulus for projectile

f_x Lateral component of internal force

f_z Axial component of internal force

F_x Lateral component of external force

F_z Axial component of external force

h   Radial location of elastic-plastic interface

I_{CG} Mass moment of inertia about CG

I_s Area moment of inertia of projectile cross section S

I_1 Material rigidity index ($\approx 2E/3Y$ for incompressible von Mises materials)

L   Projectile length

M   Projectile mass

r   Local aftbody radius; radial position in the CET

71

r_s	Projectile radius at section S
s	Axial distance from any point on aftbody to base of nose
v_x	Local lateral velocity
v_z	Local axial velocity
V_x	Lateral component of CG velocity
V_z	Axial component of CG velocity
x	Lateral distance from CG
X	Horizontal distance from origin fixed in target
$\ddot{X}, \ddot{Z}$	Components of acceleration in the X- and Z-directions, respectively
Y	Unconfined compressive strength
z	Axial distance (forward) from CG
z_n	z-coordinate of the nose tip
$z\dot{\theta}$	Lateral velocity due to pure rotation
Z	Vertical distance from origin fixed in target
α	Angle of attack
Γ	Bending moment
δ	Wake-separation gap width
ϵ_a	Axial strain
ϵ_*	Compressive radial strain at failure
η	Angle between projectile surface and projectile axis
θ	Angle of rotation
$\dot{\theta}$	Angular velocity
$\ddot{\theta}$	Angular acceleration
ξ	Variable of integration
ρ	Target mass density

σ_a Normal stress due to axial motion

σ_r Radial stress

σ_s Radial compressive stress at surface of slowly expanding spherical cavity

σ_x Lateral component of stress

$\sigma_x', \sigma_x'', \sigma_x'''$ Contributions to lateral stress due to axial, lateral, and rotational motion, respectively

σ_z Axial component of stress

$\sigma_z', \sigma_z'', \sigma_z'''$ Contributions to axial stress due to axial, lateral, and rotational motion, respectively

σ_θ Circumferential stress

ϕ Internal friction angle

ϕ_1, ϕ_2 Internal friction angle describing bilinear failure envelope

ψ Azimuthal angle, measured around projectile

73

DISTRIBUTION LIST

DEPARTMENT OF DEFENSE

Assistant to the Secretary of Defense
  Atomic Energy
    ATTN: Donald R. Cotter

Director, Defense Advanced Research
  Projects Agency
    ATTN: COL B. Pafe
          NMRO
          Paul C. McMonigal
          CDR J. Beatty
          LTC M. Franklin
          S. Lukasik
          PMO
          STO
          Eric H. Willis
          Technical Library

Director, Defense Civil Preparedness Agency
    ATTN: RE(ADM)

Defense Documentation Center,
  Cameron Station
12 cy ATTN: TC/Myer B. Kahn

Director, Defense Intelligence Agency
    ATTN: DI-7E
          DT-2, Weapons & Systems
            Division
          DI-7D, Phys. Vul. Div.,
            Edward O'Farrell
          Technical Library

Defense Mapping Agency
    ATTN: H. Lindsey

Director, Defense Nuclear Agency
    ATTN: STSI (Archives)
2 cy   STTL (Technical Library)
15 cy   SPSS
          DDST

Director of Defense Research and Engineering
    ATTN: Assistant Director, Strategic
            Weapons
          Deputy Director, Strategic
            Systems
          M. J. Minneman
          George Barse
          Craig W. Hartsell
          R. Thorkildsen
          Deputy Director, Tactical
            Warfare

Commander, Field Command, Defense Nuclear
  Agency
    ATTN: FCPR

Interservice Nuclear Weapons School
    ATTN: Technical Library

Director, Joint Strategic Target Planning
  Staff, JCS
    ATTN: Science and Technology Info
            Library
Director, Weapons Systems Evaluation Group
    ATTN: Technical Library

DEPARTMENT OF THE ARMY

Assistant Chief of Staff for Force Development
    ATTN: Director of Chem & Nuc Ops
          Technical Library

Director, U. S. Army Ballistic Missile Defense
  Advanced Technology Center
    ATTN: BMDATC-X
          CRDABH-S

Ballistic Missile Defense Program Manager
    ATTN: DACS-BMT/Dr. John Shea

Headquarters, Central Army Group
    ATTN: CENEN LTC J. L. Spruill

Office, Chief of Engineers
2 cy ATTN: DAEN-ASI-L
2 cy   DAEN-MCE-D
           DAEN-RDL

Office, Chief of Research, Development,
  and Acquisition
    ATTN: DAMA-CSM/LTC Edward V. DeBoesser, Jr.
          Technical Library

Commander, Frankford Arsenal
    ATTN: L. Baldini

Commander, Harry Diamond Laboratories
    ATTN: A. Holmes

Commander, Harry Diamond Laboratories
    ATTN: AMXDO-NP
          AMXDO-RBH/J. Gwaltney

Project Manager, Remotely Monitored Battlefield
  Sensor System
    ATTN: Chuck Higgins

Commanding Officer, Picatinny Arsenal
    ATTN: Paul Harris
          P. Angelloti
          Technical Library
          SMUPA-ND-S/E. Zimpo
          William Meyer
          Ray Goldstein
          Ray Moessner
          Marty Margolin
          Jerry Pental
          SUMPA-AD-D-A-7
          SUMPA-AD-D-A
          SUMPA-AD-D-M

Director, U. S. Army Ballistic Research
  Laboratories
    ATTN: AMXBR-X/J. J. Meszaros
          J. H. Keefer
          AMXBR-TB/J. T. Frasier
          W. J. Taylor
          Norris J. Huffington, Jr.
          D. Dunn
          G. Grabarek
          B. Reiter
          G. Roecker
2 cy   Technical Library/Edward Baicy
          J. W. Apgar

75

DEPARTMENT OF THE ARMY (Continued)

Commander/Director, U. S. Army Cold Regions
  Research and Engineering Laboratory
      ATTN: G. Swinzow

Division Engineer, U. S. Army Engineer
  Division, Huntsville
      ATTN: HNDED-CS/Michael M. Dembo

District Engineer, U. S. Army Engineer
  District, St. Paul
      ATTN: Library

Division Engineer, U. S. Army Engineer
  Division, Ohio River
      ATTN: ORDAS-L/Technical Library

Director, U. S. Army Engineer Waterways
  Experiment Station
      ATTN: Mr. L. F. Ingram
             Mr. L. K. Davis
             Mr. William J. Flathau
             Mr. John Strange
3 cy   Library
             Dr. Paul Hadala
             Dr. Guy Jackson
             Dr. Behzad Rohani
             Mr. Allen D. Rooke

Commander, U. S. Army Materials and
  Mechanics Research Center
      ATTN: John Mescall
             Technical Library
             Richard Shea

Director, U. S. Army Material Systems
  Analysis Agency
      ATTN: J. Sperazza
             M. Reches

Commander, U. S. Army Mobility Equipment
  R&D Center
      ATTN: STSFB-MW
             STSFB-XS
             Technical Library

Commandant, U. S. Army Engineer School
      ATTN: ATSEN-SY-L

Commander, U. S. Army Materiel Development
  and Readiness Command, (DARCOM)
      ATTN: Technical Library

Commander, U. S. Army Materiel Development
  and Readiness Command, (DARCOM)
      ATTN: Research and Concepts Branch

Commander, U. S. Army Nuclear Agency
      ATTN: Document Control
             Technical Library
             COL Quinn
             MAJ F. P. Weichel

Commander, U. S. Army Missile Command
      ATTN: Technical Library
             F. Fleming
             AMCPM-PE-X (William K. Jann)

DEPARTMENT OF THE ARMY (Continued)

Commander, U. S. Army Armament Command
      ATTN: Technical Library

Division Engineer, U. S. Army Engineer
  Division, Missouri River
      ATTN: Library

DEPARTMENT OF THE NAVY

Chief of Naval Research, Department of
  the Navy
      ATTN: Technical Library

Officer in Charge, Civil Engineering Laboratory,
  Naval Construction Battalion Center
      ATTN: R. J. Odello
             Technical Library

Commander, Naval Electronics Systems Command
      ATTN: PME-117-21A

Commander, Naval Facilities Engineering Command
      ATTN: Technical Library, Code 0911C

Superintendent, U. S. Naval Postgraduate School
      ATTN: Library, Code 2124

Director, Naval Research Laboratory
      ATTN: Code 2027/Tech Library

Commander, Naval Surface Weapons Center
      ATTN: Mr. Kasdorf
             Technical Library, Code 730
             Code 1224 Navy Nuc Prgms Off
             Jules Enig
             Mary P. King
             L. Roslund
             Robert D. Heidenreich
             G. Briggs

Commander, Naval Surface Weapons Center
  Dahlgren Laboratory
      ATTN: Technical Library
             William Wisherd
             Ted Williams
             M. Weiland

Commander, Naval Weapons Center
      ATTN: Code 603, Dr. Carl Austin
             Mr. P. Cordle
             Code 533, Technical Library

Commander, Naval Weapons Evaluation Facility,
  Kirtland Air Force Base
      ATTN: Technical Library

Director, Strategic Systems Project Office
      ATTN: NSP-43, Technical Library

DEPARTMENT OF THE AIR FORCE

Air Force Armament and Testing Laboratory, AFSC
      ATTN: Technical Library
             MAJ Thomas Tomasetti
             Mr. John Collins
             Mr. Leonard Wilson
             Mr. Masey Valentine
             Mr. William Cramer
             Dr. Kulp

DEPARTMENT OF THE AIR FORCE (Continued)

Air Force Institute of Technology
ATTN: Technical Library

Commander, Air Force Weapons Laboratory
ATTN: SUL, Technical Library
DEV-S/Dr. M. A. Plamondon

Headquarters, Air Force Systems Command
ATTN: Technical Library

Project Manager, Gator Mine Program
ATTN: E. J. Lindsey

Oklahoma State University
Field Office for Weapons Effectiveness
ATTN: Ed Jackett

Air Force Office of Scientific Research
ATTN: LTC L. P. Mosteller, Jr.

Commander, Rome Air Development Center
ATTN: EMTLD, Documents Library

Commander, Armament Development and Test
Center
ATTN: ADTC/DLODL/Technical Library

Commander, Foreign Technology Division
ATTN: TD-BTA Library

HQ USAF/IN
ATTN: INATA

HQ USAF/RD
ATTN: RDPM, COL J. E. McCormick

Space and Missile Systems Organization
ATTN: DEB

ENERGY RESEARCH & DEVELOPMENT ADMINISTRATION

U. S. Energy Research and Development
Administration, Division of Military
Application
ATTN: Doc Control for Test Office

U. S. Energy Research and Development Ad-
ministration, Albuquerque Operations Office
ATTN: Doc Control for Technical Library

U. S. Energy Research and Development
Administration, Division of Headquarters
Services
ATTN: Doc Control for Class Tech Lib

U. S. Energy Research and Development
Administration, Nevada Operations Office
ATTN: Doc Control for Technical Library

Los Alamos Scientific Laboratory
ATTN: Doc Control for Reports Library
Doc Control for Tom Dowler
Doc Control for C. Cremer
Doc Control for G. Dials

Sandia Laboratories, Livermore Laboratory
ATTN: Doc Control for T. Gold
Doc Control for Technical Library

ENERGY RESEARCH & DEVELOPMENT
ADMINISTRATION (Continued)

Sandia Laboratories
ATTN: Doc Control for Dr. Walter Herrmann
Doc Control for John Colp
Doc Control for John Keizur
Org. No. 1312
Doc Control for William Patterson
Doc Control for Al Chabai
Doc Control for 3141 Sandia Rpt Coll
Doc Control for Ray Reynolds

Director, Lawrence Livermore Laboratory
ATTN: Technical Information Division,
Technical Library
Larry Woodruff, L-125
Doc Control for W. Scanlin
Frank Walker
Mark Wilkins

OTHER GOVERNMENT AGENCIES

Electric Power Research Institute
ATTN: Dr. George Sliter

Office of Nuclear Reactor Regulation,
Nuclear Regulatory Commission
ATTN: Mr. Lawrence Shao, Chief,
Struc Engrg Br

Bureau of Mines, Twin Cities Research Center
ATTN: R. E. Thill

DEPARTMENT OF DEFENSE CONTRACTORS

Aerospace Corporation
ATTN: Technical Information Services
R. Strickler
George Young

Agbabian Associates
ATTN: Dr. M. S. Agbabian

Applied Theory Incorporated
2 cy ATTN: Dr. John G. Trulio

AVCO, Government Products Group
ATTN: David Henderson
Frank Lasher
Research Library A830, Room 7201
John Atanasoff

Battelle Columbus Laboratories
ATTN: Technical Library

Bell Telephone Laboratories, Inc.
ATTN: Technical Report Center

Boeing Company
ATTN: Aerospace Library
Reynold Atlas

California Research and Technology, Inc.
ATTN: Dr. K. N. Kreyenhagen
Technical Library

Civil/Nuclear Systems Corporation
ATTN: Robert Crawford

77

EG&G, Inc., Albuquerque Division
    ATTN: Technical Library

General Dynamics Corporation, Pomona Operation
    ATTN: Keith Anderson

General Electric Company, TEMPO-Center
  for Advanced Studies
    ATTN: DASIAC

IIT Research Institute
    ATTN: Technical Library

Institute for Defense Analyses
    ATTN: IDA Librarian Ruth S. Smith

Consulting and Special Engineering Services
    ATTN: Dr. J. L. Merritt
          Technical Library

Kaman Avidyne, Division of Kaman Sciences Corp.
    ATTN: Technical Library
          E. S. Crisicone
          N. P. Hobbs

Kaman Sciences Corporation
    ATTN: Technical Library

Lockheed Missiles and Space Company
    ATTN: Tech Info Center D/Coll

Lockheed Missiles and Space Company
    ATTN: Technical Library

Martin Marietta Aerospace, Orlando Division
    ATTN: M. Anthony
          Gerbert E. McQuaig (MP-81)

University of Illinois
    ATTN: Dr. Nathan M. Newmark

University of New Mexico,
  Dept of Campus Security and Police
    ATTN: H. D. Southward
          G. E. Triandafalidis

Physics International Company
    ATTN: Doc Control for Mr. Fred M. Sauer
          Doc Control for Dr. Robert Swift
          Doc Control for Technical Library
          Doc Control for Mr. Dennis L. Orphal
          Doc Control for Mr. Larry Behrman

R&D Associates
    ATTN: Dr. Harold L. Brode
          Dr. H. F. Cooper, Jr.
          Mr. R. J. Port
          Technical Library
          Mr. William B. Wright
          Dr. C. P. Knowles
          Mr. J. G. Lewis

Science Applications, Inc.
    ATTN: Mr. David Bernstein
          Dr. D. E. Maxwell
          Dr. Cecil Ivan Hudson, Jr.
          Dr. W. M. Layson

Stanford Research Institute
    ATTN: Dr. Carl Peterson
          Dr. G. Abrahamson
          Mr. Lynn Seamans
          SRI Library Room G021

Systems, Science and Software
    ATTN: Dr. Donald R. Grine
          Dr. E. W. Gaffney
          Technical Library

Terra Tek, Inc.
    ATTN: Mr. S. J. Green
          Dr. A. H. Jones
          Technical Library

Texas A&M University
    ATTN: Harry Coyle

Texas A&M University
    ATTN: Prof. L. J. Thompson

Braddock, Dunn, & McDonald, Inc.
    ATTN: Technical Library

TRW Defense and Space Systems Group
    ATTN: Tech Info Center/S-1930

Weidlinger Associates, Consulting Engineers
    ATTN: Dr. Melvin L. Baron
          Mr. J. W. Wright

Weidlinger Associates, Consulting Engineers
    ATTN: Dr. J. Isenberg

Lowell Technical Institute,
  Department of Civil Engineering
    ATTN: L. W. Thigpen

Georgia Institute of Technology,
  Department of Aerospace Engineering
    ATTN: S. V. Hanagud
          L. N. Rehfield

Engineering Societies Library
    ATTN: Miss Anne Mott, Acquisitions
          Librarian

Pacifica Technology, Inc.
    ATTN: G. I. Kent
          R. L. Bjork

FOREIGN EXCHANGES

Regierungsrat, Bundesanstalt fur Strassenwesen

Department of Physical Geography, Uppsala
University

Prof. Leopold Muller, Abteilung Felsmechanik,
  Institut fur Bodenmechanik und Felsmechanik,
  Universitat Karlsruhe

DOMESTIC EXCHANGE

Tennessee Valley Authority
    ATTN: Ronald G. Domer, Chief, Civil
          Engineering Branch

DEPARTMENT OF DEFENSE	DEPARTMENT OF THE ARMY

DEPARTMENT OF DEFENSE

Assistant to the Secretary of Defense
Atomic Energy
    ATTN: Donald R. Cotter

Director, Defense Advanced Research
Projects Agency
    ATTN: COL B. Pafe
           NMRO
           Paul C. McMonigal
           CDR J. Beatty
           LTC M. Franklin
           S. Lukasik
           PMO
           STO
           Eric H. Willis
           Technical Library

Director, Defense Civil Preparedness Agency
    ATTN: RE(ADM)

Defense Documentation Center,
Cameron Station
12 cy ATTN: TC/Myer B. Kahn

Director, Defense Intelligence Agency
    ATTN: DI-7E
           DT-2, Weapons & Systems
             Division
           DI-7D, Phys. Vul. Div.,
             Edward O'Farrell
           Technical Library

Defense Mapping Agency
    ATTN: H. Lindsey

Director, Defense Nuclear Agency
    ATTN: STSI (Archives)
2 cy   STTL (Technical Library)
15 cy   SPSS
           DDST

Director of Defense Research and Engineering
    ATTN: Assistant Director, Strategic
             Weapons
           Deputy Director, Strategic
             Systems
           M. J. Minneman
           George Barse
           Craig W. Hartsell
           R. Thorkildsen
           Deputy Director, Tactical
             Warfare

Commander, Field Command, Defense Nuclear
Agency
    ATTN: FCPR

Interservice Nuclear Weapons School
    ATTN: Technical Library

Director, Joint Strategic Target Planning
Staff, JCS
    ATTN: Science and Technology Info
             Library
Director, Weapons Systems Evaluation Group
    ATTN: Technical Library

DEPARTMENT OF THE ARMY

Assistant Chief of Staff for Force Development
    ATTN: Director of Chem & Nuc Ops
           Technical Library

Director, U. S. Army Ballistic Missile Defense
Advanced Technology Center
    ATTN: BMDATC-X
           CRDABH-S

Ballistic Missile Defense Program Manager
    ATTN: DACS-BMT/Dr. John Shea

Headquarters, Central Army Group
    ATTN: CENEN LTC J. L. Spruill

Office, Chief of Engineers
2 cy   ATTN: DAEN-ASI-L
2 cy   DAEN-MCE-D
           DAEN-RDL

Office, Chief of Research, Development,
and Acquisition
    ATTN: DAMA-CSM/LTC Edward V. DeBoesser, Jr.
           Technical Library

Commander, Frankford Arsenal
    ATTN: L. Baldini

Commander, Harry Diamond Laboratories
    ATTN: A. Holmes

Commander, Harry Diamond Laboratories
    ATTN: AMXDO-NP
           AMXDO-RBH/J. Gwaltney

Project Manager, Remotely Monitored Battlefield
Sensor System
    ATTN: Chuck Higgins

Commanding Officer, Picatinny Arsenal
    ATTN: Paul Harris
           P. Angelloti
           Technical Library
           SMUPA-ND-S/E. Zimpo
           William Meyer
           Ray Goldstein
           Ray Moessner
           Marty Margolin
           Jerry Pental
           SUMPA-AD-D-A-7
           SUMPA-AD-D-A
           SUMPA-AD-D-M

Director, U. S. Army Ballistic Research
Laboratories
    ATTN: AMXBR-X/J. J. Meszaros
           J. H. Keefer
           AMXBR-TB/J. T. Frasier
           W. J. Taylor
           Norris J. Huffington, Jr.
           D. Dunn
           G. Grabarek
           B. Reiter
           G. Roecker
2 cy   Technical Library/Edward Baicy
           J. W. Apgar

In accordance with letter from DAEN-RDC, DAEN-ASI dated
22 July 1977, Subject: Facsimile Catalog Cards for
Laboratory Technical Publications, a facsimile catalog
card in Library of Congress MARC format is reproduced
below.